Int J Fract (2006) 141:291–312
DOI 10.1007/s10704-006-0083-6

ORIGINAL ARTICLE

A failure criterion for brittle elastic materials under mixed-mode loading

Zohar Yosibash · Elad Priel · Dominique Leguillon

Received: 12 January 2006 /Accepted: 15 May 2006

Abstract The failure criterion of Leguillon at reentrant corners in brittle elastic materials (Leguillon 2002, Eur J Mech A/Solids 21: 61–72; Leguillon et al. (2003), Eur J Mech A—Solids 22(4): 509–524) validated in (Yosibash et al. 2004, Int J Fract 125(3–4): 307–333) for mode I loading is being extended to mixed mode loading and is being validated by experimental observations. We present an explicit derivation of all quantities involved in the computation of the failure criterion. The failure criterion is validated by predicting the critical load and crack initiation angle of specimens under mixed mode loading and comparison to experimental observations on PMMA (polymer) and Macor (ceramic) V-notched specimens.

Keywords Failure initiation · Mixed-mode fracture · Generalized stress intensity factors · V-notch

Z. Yosibash (✉) · E. Priel
Pearlstone Center for Aeronautical Engineering Studies, Department of Mechanical Engineering, Ben-Gurion University of the Negev, Beer-Sheva 84105, Israel
e-mail: zohary@bgumail.bgu.ac.il

D. Leguillon
LMM-CNRS UMR7607, Universite Pierre et Marie Curie, 75252 Paris Cedex 05 France
e-mail: dol@ccr.jussieu.fr

1 Introduction

Failure laws for brittle materials containing V-notches of variable opening angles, multi-material interfaces or orthotropic materials have become of major interest because of failure initiation phenomena that occur in composite materials and electronic devices (see, e.g. Mohammed and Liechti 2000; Yosibash et al. 2003). A reliable law for predicting the failure initiation instance (crack formation) in these cases in the vicinity of singular points, especially when a complex state of stress is present in the vicinity of the V-notch tip, is still a topic of active research and interest. At such points the stress tensor is infinity under the assumption of linear elasticity. A typical example of a singular point is the V-notch tip, for which a crack tip is a particular case when the V-notch solid angle is 2π.

For the simplified mode I state of stresses in the vicinity of a V-notch tip, i.e. tension perpendicular to the V-notch bi-sector alone, several failure criteria have been proposed and verified by experimental observations, as in Dunn et al. (1977a), Fett (1996), Lazzarin and Zmabardi (2001), Leguillon (2002), and Seweryn (1994). A comparison of several of the presented failure criteria (and a newly proposed one) against experimental observations is presented in Yosibash et al (2004).

For a mixed mode stress state in the vicinity of a V-notch tip, the number of failure initiation criteria suggested and validated via experimental

observations is much smaller. Among these are (Dunn et al. 1977b; Labossiere et al. 2002; Seweryn and Lukaszewicz 2002; Seweryn et al. 1997). The failure criterion in Dunn et al. (1997b) for brittle isotropic materials is based on the mode I generalized stress intensity factor (GSIF) and is restricted to low values of mode mixity when mode I dominates. This failure criterion is being also applied to a V-notch at a silicon/glass bimaterial interface (Labossiere et al. 2002), correlating mode I GSIF to the experimental observations for two V-notch opening angles. It is difficult to ascertain precisely the effect of mode mixity from the results in Labossiere et al. (2002) because the change in mode mixity is relatively small for one V-notch opening angle, and there is no systematic dependence of the failure load on mixity measure for the other V-notch opening angle. The failure criteria investigated by Seweryn et al. (1997) although predicting well the failure initiation, have been shown to be inferior to Leguillon's criterion for mode I loading. Therefore, we herein extend the failure criterion presented by Leguillon (2002), based on finite fracture mechanics concept, to mixed mode loading. This criterion, shown to predict very well failure initiation under mode I loading for various V-notch angles (see, e.g. Leguillon 2002; Leguillon and Yosibash 2003), satisfies both the classical Griffith criterion and the strength criterion. It relies on the linear elastic asymptotic solution in the vicinity of a sharp V-notch tip, and the assumption of small-scale cracking (see, e.g. Dunn et al. 2001; Reedy 2000), applicable to relatively brittle materials. In Dunn et al. (2001) and Reedy (2000) the linear elastic solution in the vicinity of a V-notch tip which is perturbed by geometric discontinuities (small cracks, holes, etc.) and/or plasticity is shown to be controlled by the leading terms of the asymptotic solution for the corresponding unperturbed sharp V-notch tip.

We consider a domain containing a V-notch with a solid angle ω (so that the opening angle is $2\pi - \omega$) with a small crack of length ℓ that initiates at an angle θ_0, see Fig. 1. Following Leguillon's failure initiation criterion for mode I loading (Leguillon 2001) and the preliminary work (Leguillon and Siruguet 2002), we extend it herein to a mixed mode loading, and validate it by experimental observations. The failure criterion depends on two material

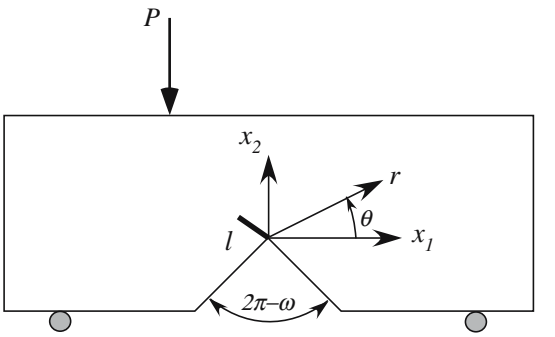

Fig. 1 The V-notched specimen with a crack at its tip

parameters, the 1-D stress at brittle fracture, σ_c (strength), and the fracture energy release rate per a unit surface f, G_c (toughness), the first two generalized stress intensity factors A_1 and A_2 associated with the V-notch tip and three geometrical functions H_{11}, H_{12}, H_{22} that depend on the V-notch geometry alone.

Preliminaries and notations, including the stress and displacement fields in the vicinity of a V-notch tip in two-dimensional elastic isotropic domains, are provided in Sect. 2. Thereafter we perform an asymptotic analysis that provides the change in potential energy in a V-notch domain due to a small crack of length ℓ that initiates at it's tip in Sect. 3. This analysis presents three new geometrical functions and detailed numerical methods for their computation, followed by the explicit derivation of failure criterion. In Sect. 4, we use the p-version of the finite element method to compute the required geometrical functions, and verify that indeed the asymptotic analysis for the difference in potential energy holds true. Finally, the failure criterion is validated by comparing the predicted failure load and crack initiation angles to experimental observations on V-notched specimens made of PolyMethil Metacrylate (PMMA) and Machinable Ceramics (Macor) in Sect. 5. Both tests reported in the literature and new ones performed by us are considered, having a large mode mixity variation. Summary and conclusions are provided in Sect. 6.

2 Preliminaries and notations

The displacements and stresses in the vicinity of a traction free V-notch tip can be expressed by an asymptotic series which is provided in this section.

In the literature (see Szabó and Babuška 1988) the asymptotic series is usually expressed in a cylindrical coordinate system, which is rotated by $\pi/2$ radians in respect to the coordinate system shown in Fig. 1. To distinguish between the two coordinate systems the one used in this section is marked with an asterics, i.e. $\theta^* = \theta - \pi/2$, see Fig. 2.

The displacements in the vicinity of the V-notch tip are expressed as a series, for which the first three terms are given by:

$$\begin{aligned}\boldsymbol{u}(r,\theta) \overset{\text{def}}{=} \begin{Bmatrix} u_r \\ u_\theta \end{Bmatrix} &= \boldsymbol{u}(0,0) \\ &+ A_1 r^{\alpha_1} \begin{Bmatrix} \left[\cos(1+\alpha_1)\theta^* + \frac{[\lambda+3\mu-\alpha_1(\lambda+\mu)]}{(\lambda+\mu)(1-\alpha_1)} \frac{\sin[\omega(1+\alpha_1)/2]}{\sin[\omega(1-\alpha_1)/2]} \cos(1-\alpha_1)\theta^*\right] / \left(2\mu\alpha_1\sigma^{\mathrm{I}}_{\theta\theta}(\theta^*=0)\right) \\ \left[-\sin(1+\alpha_1)\theta^* - \frac{[\lambda+3\mu+\alpha_1(\lambda+\mu)]}{(\lambda+\mu)(1-\alpha_1)} \frac{\sin[\omega(1+\alpha_1)/2]}{\sin[\omega(1-\alpha_1)/2]} \sin(1-\alpha_1)\theta^*\right] / \left(2\mu\alpha_1\sigma^{\mathrm{I}}_{\theta\theta}(\theta^*=0)\right) \end{Bmatrix} \\ &+ A_2 r^{\alpha_2} \begin{Bmatrix} \left[\sin(1+\alpha_2)\theta^* + \frac{[\lambda+3\mu-\alpha_2(\lambda+\mu)]}{(\lambda+\mu)(1+\alpha_2)} \frac{\sin[\omega(1+\alpha_2)/2]}{\sin[\omega(1-\alpha_2)/2]} \sin(1-\alpha_2)\theta^*\right] / \left(2\mu\alpha_2\sigma^{\mathrm{II}}_{r\theta}(\theta^*=0)\right) \\ \left[\cos(1+\alpha_2)\theta^* + \frac{[\lambda+3\mu+\alpha_2(\lambda+\mu)]}{(\lambda+\mu)(1+\alpha_2)} \frac{\sin[\omega(1+\alpha_2)/2]}{\sin[\omega(1-\alpha_2)/2]} \cos(1-\alpha_2)\theta^*\right] / \left(2\mu\alpha_2\sigma^{\mathrm{II}}_{r\theta}(\theta^*=0)\right) \end{Bmatrix} \end{aligned} \quad (1)$$

where $\boldsymbol{u}(0,0)$ is the rigid body displacement of the V-notch tip and the corresponding first two terms of the stress tensor in polar coordinates are:

$$\begin{aligned}\boldsymbol{\sigma} = \begin{Bmatrix} \sigma_{rr} \\ \sigma_{\theta\theta} \\ \sigma_{r\theta} \end{Bmatrix} &= A_1 r^{\alpha_1-1} \begin{Bmatrix} \left[\cos(1+\alpha_1)\theta^* + \frac{(3-\alpha_1)}{(1-\alpha_1)} \frac{\sin[\omega(1+\alpha_1)/2]}{\sin[\omega(1-\alpha_1)/2]} \cos(1-\alpha_1)\theta^*\right] / \sigma^{\mathrm{I}}_{\theta\theta}(\theta^*=0) \\ \left[-\cos(1+\alpha_1)\theta^* + \frac{(1+\alpha_1)}{(1-\alpha_1)} \frac{\sin[\omega(1+\alpha_1)/2]}{\sin[\omega(1-\alpha_1)/2]} \cos(1-\alpha_1)\theta^*\right] / \sigma^{\mathrm{I}}_{\theta\theta}(\theta^*=0) \\ \left[-\sin(1+\alpha_1)\theta^* + \frac{\sin[\omega(1+\alpha_1)/2]}{\sin[\omega(1-\alpha_1)/2]} \sin(1-\alpha_1)\theta^*\right] / \sigma^{\mathrm{I}}_{\theta\theta}(\theta^*=0) \end{Bmatrix} \\ &+ A_2 r^{\alpha_2-1} \begin{Bmatrix} \left[\sin(1+\alpha_2)\theta^* + \frac{(3-\alpha_2)}{(1+\alpha_2)} \frac{\sin[\omega(1+\alpha_2)/2]}{\sin[\omega(1-\alpha_2)/2]} \sin(1-\alpha_2)\theta^*\right] / \sigma^{\mathrm{II}}_{r\theta}(\theta^*=0) \\ \left[-\sin(1+\alpha_2)\theta^* + \frac{\sin[\omega(1+\alpha_2)/2]}{\sin[\omega(1-\alpha_2)/2]} \sin(1-\alpha_2)\theta^*\right] / \sigma^{\mathrm{II}}_{r\theta}(\theta^*=0) \\ \left[\cos(1+\alpha_2)\theta^* - \frac{(1-\alpha_2)}{(1+\alpha_2)} \frac{\sin[\omega(1+\alpha_2)/2]}{\sin[\omega(1-\alpha_2)/2]} \cos(1-\alpha_2)\theta^*\right] / \sigma^{\mathrm{II}}_{r\theta}(\theta^*=0) \end{Bmatrix}. \end{aligned} \quad (2)$$

In (1–3), we have used the following notations:

$$\sigma^{\mathrm{I}}_{\theta\theta}(\theta^*=0) \overset{\text{def}}{=} \frac{(1+\alpha_1)}{(1-\alpha_1)} \frac{\sin[\omega(1+\alpha_1)/2]}{\sin[\omega(1-\alpha_1)/2]} - 1, \quad (3)$$

$$\sigma^{\mathrm{II}}_{r\theta}(\theta^*=0) \overset{\text{def}}{=} 1 - \frac{(1-\alpha_2)}{(1+\alpha_2)} \frac{\sin[\omega(1+\alpha_2)/2]}{\sin[\omega(1-\alpha_2)/2]} \quad (4)$$

in order to normalize the "eigen-stresses" so that for mode I

$$\sigma^{\mathrm{I}}_{\theta\theta}(\theta^*=0) = 1$$

and for mode II:

$$\sigma^{\mathrm{II}}_{r\theta}(\theta^*=0) = 1$$

then $\sigma_{\theta\theta}(r,\theta^*=0) = A_1 r^{\alpha_1-1}$ and $\sigma_{r\theta}(r,\theta^*=0) = A_2 r^{\alpha_2-1}$.

The two "eigen-values" α_1 and α_2 are the smallest roots of the characteristic equations;

$$\sin(\alpha_1\omega) + \alpha_1 \sin(\omega) = 0, \quad (5)$$

$$\sin(\alpha_2\omega) - \alpha_2 \sin(\omega) = 0. \quad (6)$$

For a crack ($\omega = 2\pi$) the Eqs. 5 and 6 are identical and the first two roots are real and simple $\alpha_1 = \alpha_2 = 1/2$. In this case the "classical" mode I and II stresses and displacements for a crack, well known in fracture mechanics (Kanninen and Popelar 1985), are obtained and the coefficients A_1 and A_2 are related to the stress intensity $A_1 = K_{\mathrm{I}}/\sqrt{2\pi}$, $A_2 = K_{\mathrm{II}}/\sqrt{2\pi}$. When $\omega \neq 2\pi$, then not all roots are real and multiple roots may exist. From the engineering viewpoint, V-notch solid angles up to $4\pi/3$ (240°) are of greatest importance and in this cases the smallest roots are real — see a summary in Table 1.

For a V-notch solid angle smaller than 1.43028π (257.45°), then $\alpha_2 > 1$ and the mode II stress com-

Table 1 First two eigen-values for selected angles ω

Solid angle ω	2π (crack)	$11\pi/6(330°)$	$7\pi/4(315°)$	$5\pi/3(300°)$	$3\pi/2(270°)$	$4\pi/3(240°)$
α_1	1/2	0.5014530	0.5050097	0.5122214	0.5444837	0.6157311
α_2	1/2	0.5981918	0.6597016	0.7309007	0.9085292	1.148913

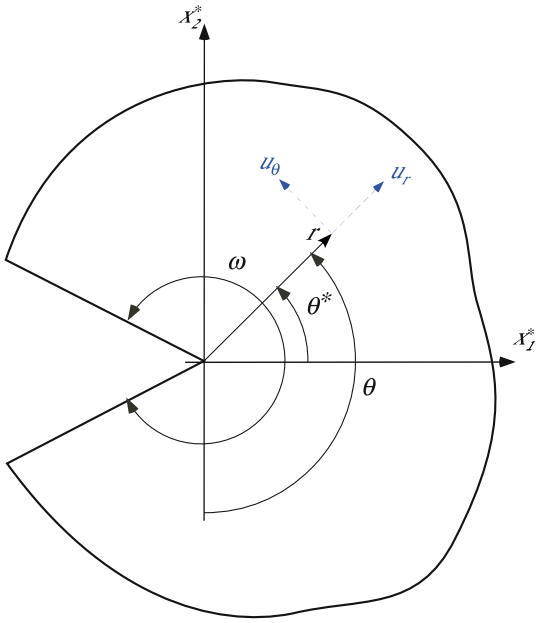

Fig. 2 The coordinate system at the V-notched tip

ponents are bounded, whereas mode I stress components are bounded for $\omega < \pi$.

As an example we present in Fig. 3 the eigen-stresses and in the four eigen-displacements for mode I and mode II for a V-notch with a solid angle of $\omega = 7\pi/4$, and $E = 1$ and $\nu = 0.36$.

3 The failure initiation criterion for mixed mode loading

We extend Leguillon's failure criterion to mixed mode loading and provide explicit formulae for the determination of the various entities required for its formulation. The corner-stone of this criterion is the postulate that a finite crack length ℓ_0 has to be instantaneously created so to satisfy both the strength and toughness requirements. For a given small load, a large crack is required to satisfy the toughness criterion, whereas only at small distance from the notch tip the tangential stress reaches σ_c (the strength criterion is satisfied). To satisfy both criteria simultaneously, the load has to be increased so that the upper bound of the crack length decreases to satisfy the toughness criterion, and the distance from the notch tip where tangential stress reaches σ_c increases. Only when the load is increased to a level where the lower bound of a crack to satisfy the toughness criterion equals the upper bound of the distance to satisfy the stress criterion, a crack of this length is crated satisfying simultaneously the two criteria.

To this end let us first consider the Griffith energy criterion as it is manifested for *finite fracture mechanics* (Hashin 1996; Taylor et al. 2005) when a *small crack* of length ℓ_0 is spontaneously formed at a V-notch tip. In this case, for a crack to be formed the following inequality has to hold:

$$\frac{-\delta\Pi}{\ell} \geq G_c, \tag{7}$$

where $\delta\Pi$ denotes the difference in the potential energy between a V-notched cracked domain and the V-notched un-cracked domain:

$$-\delta\Pi \stackrel{\text{def}}{=} -(\Pi(\ell) - \Pi(\ell = 0)) \tag{8}$$

and $G_c = \frac{K_{Ic}^2}{E/(1-\nu^2)}$ for plane strain.

By an asymptotic analysis, we prove in the following that:

$$\begin{aligned} -\delta\Pi &= -(\Pi(\ell) - \Pi(0)) \\ &= A_1^2 H_{11}(\ell,\theta_0)\ell^{2\alpha_1} + A_1 A_2 H_{12}(\ell,\theta_0)\ell^{\alpha_1+\alpha_2} \\ &\quad + A_2^2 H_{22}(\ell,\theta_0)\ell^{2\alpha_2} + \cdots \end{aligned} \tag{9}$$

where $-\delta\Pi$ is expressed in terms of A_i, ℓ and newly defined "Geometrical factors" named H_{ij} which are defined in the sequel Fig. 4.

3.1 An asymptotic analysis for a V-notch tip with a crack at an angle θ_0

In the following section, we provide an asymptotic analysis of the displacement field when a small finite crack is introduced at the V-notch tip. Let us denote the solution (displacements and stresses) to the elasticity problem shown in Fig. 1 by $\boldsymbol{u}_\ell$

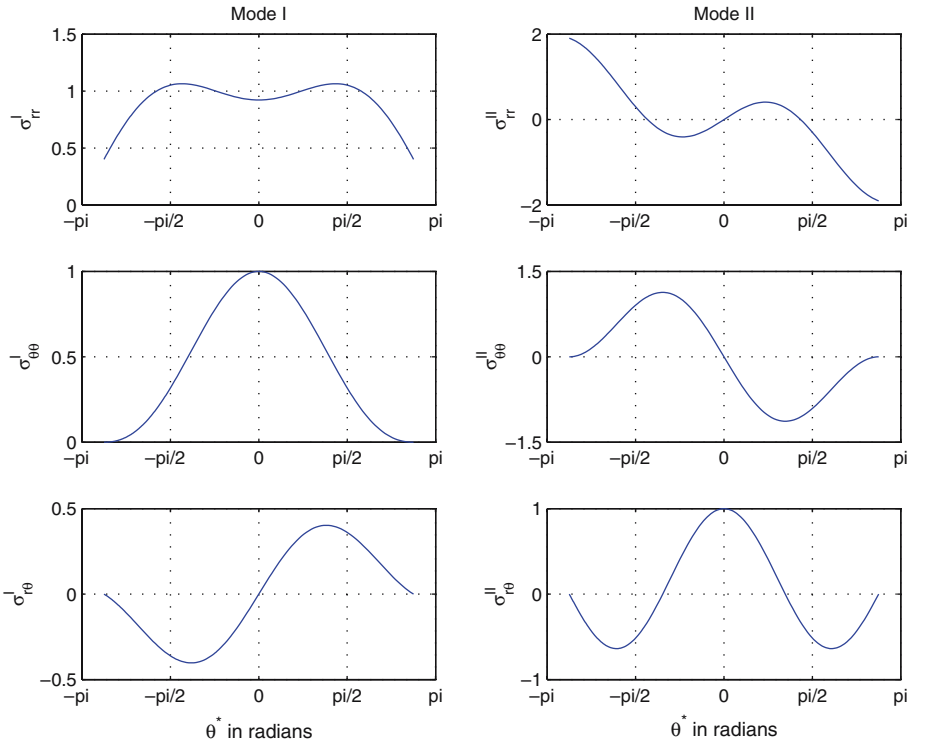

Fig. 3 Modes I and II Polar eigen-stresses for the $7\pi/4$ V-notch

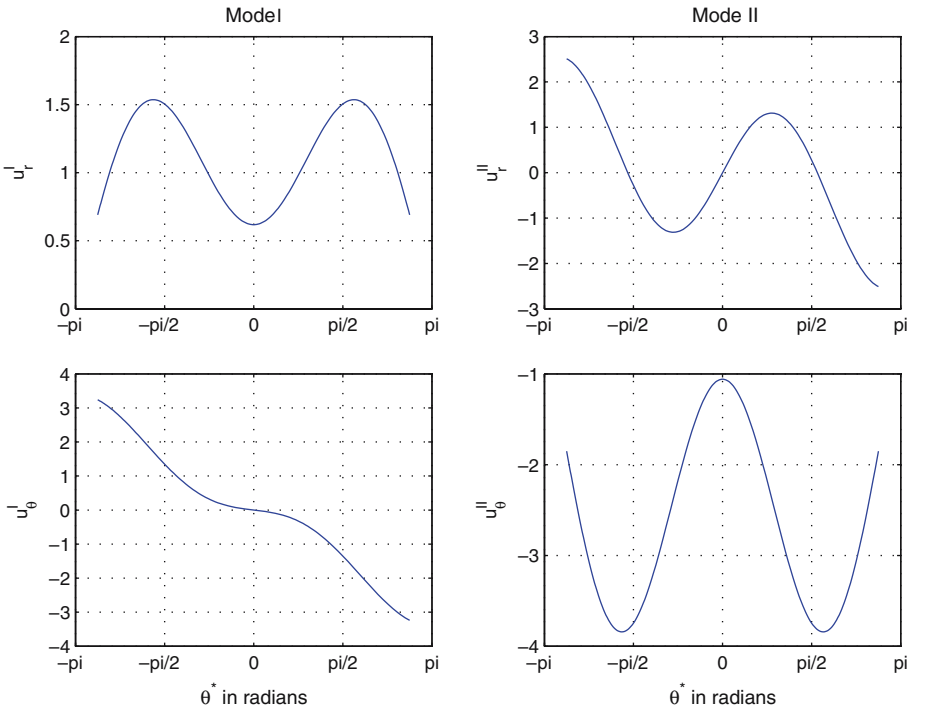

Fig. 4 Modes I and II polar eigen-displacements for the $7\pi/4$ V-notch

and $\boldsymbol{\sigma}_\ell$. If the crack is small enough compared to the dimensions of the V-notch and the specimen, and if one moves away from the V-notch tip, an *outer expansion* of the solution is obtained assuming $\ell \to 0$, which is the solution in the vicinity of a V-notch given in (1) and (3), written in a more compact form as:

$$\boldsymbol{u}(r,\theta) \stackrel{\text{def}}{=} \begin{Bmatrix} u_r \\ u_\theta \end{Bmatrix}_0 = \boldsymbol{u}(0,0) + \sum_{i=1}^{L} A_i\, r^{\alpha_i} \boldsymbol{u}^{(i)}(\theta) + \text{smaller order terms}, \tag{10}$$

$$\boldsymbol{\sigma}(r,\theta) \stackrel{\text{def}}{=} \begin{Bmatrix} \sigma_{rr} \\ \sigma_{\theta\theta} \\ \sigma_{r\theta} \end{Bmatrix}_0 = \sum_{i=1}^{L} A_i\, r^{\alpha_i - 1} \boldsymbol{\sigma}^{(i)}(\theta) + \text{smaller order terms}, \tag{11}$$

where $\boldsymbol{u}(0,0)$ denotes a constant displacement of the notch tip, and α_i and $\boldsymbol{u}^{(i)}(\theta)$ are the eigen-pairs, which satisfy each the equilibrium equation and the traction free boundary conditions on Γ_1 and Γ_2.

On the other hand, "looking at" the very close neighborhood of the V-notch tip, i.e. if a coordinate transform of the form: $y_i = x_i/\ell$ is performed, the *inner expansion* of the solution can be computed. In this case, the solution is ℓ dependent, and the small crack of length ℓ becomes of length 1 in the stretched coordinate, and the domain of interest becomes unbounded in terms of $\rho = r/\ell$. The solution, in the unbounded domain, denoted by $\boldsymbol{u}_l$ can be represented as:

$$\boldsymbol{u}_\ell(\ell y_1, \ell y_2) = d_0(\ell)\boldsymbol{v}_0(y_1,y_2) + d_1(\ell)\boldsymbol{v}_1(y_1,y_2) + d_2(\ell)\boldsymbol{v}_2(y_1,y_2) + \cdots \tag{12}$$

with

$$\lim_{\ell\to 0} \frac{d_{i+1}(\ell)}{d_i(\ell)} = 0$$

In Fig. 5 the Outer/Inner expansion domains are shown. To evaluate the various expressions in (12), we need to determine what are the boundary condition that (12) has to satisfy as $\rho \to \infty$. These in turn are obtained from the outer expansion as $r \to 0$. Expressing $\boldsymbol{u}$ in (10) in ρ coordinates:

$$\boldsymbol{u} = \boldsymbol{u}(0,0) + A_1\, \ell^{\alpha_1} \rho^{\alpha_1} \boldsymbol{u}^{(1)}(\theta) + A_2\, \ell^{\alpha_2} \rho^{\alpha_2} \boldsymbol{u}^{(2)}(\theta) + \text{higher order terms}. \tag{13}$$

We may now match each term in (12) as $\rho \to \infty$ with each of the terms in (13).

First term

One notices that if $d_1(\ell) = 1$ and $\boldsymbol{v}_0(y_1,y_2) = \boldsymbol{u}(0,0) = \begin{Bmatrix} c_1 \\ c_2 \end{Bmatrix}$ then $\boldsymbol{v}_0(y_1,y_2)$ satisfies both equilibrium equation and traction free boundary conditions on $\Gamma_i, i = 1,2,3,4$, and as $\rho \to \infty$ one obtains that:

$$d_0(\ell)\boldsymbol{v}_0(y_1,y_2) = \begin{Bmatrix} c_1 \\ c_2 \end{Bmatrix} \underset{\rho\to\infty}{\Rightarrow} \boldsymbol{u}(0,0).$$

Second term

If $d_1(\ell) = A_1\, \ell^{\alpha_1}$ and

$$\boldsymbol{v}_1(y_1,y_2) \sim \rho^{\alpha_1} \boldsymbol{u}^{(1)}(\theta) \quad \text{as } \rho \to \infty \tag{14}$$

then, we may match the inner and outer expansions as $\rho \to \infty$, and $r \to 0$.

A major difficulty to solve for $\boldsymbol{v}_1$ above is the fact that it tends to infinity as $\rho \to \infty$, thus it's strain energy is unbounded. Therefore, let us represent

$$\boldsymbol{v}_1(y_1,y_2) = \rho^{\alpha_1} \boldsymbol{u}^{(1)}(\theta) + \hat{\boldsymbol{v}}_1(y_1,y_2). \tag{15}$$

In this case $\hat{\boldsymbol{v}}_1 \to 0$ as $\rho \to \infty$, and the limit of $\boldsymbol{v}_1$ as in (15), is satisfied. Thus, to obtain $\boldsymbol{v}_1$ one needs to solve for $\hat{\boldsymbol{v}}_1$ the following elasticity problem:

$$\begin{aligned} \mathcal{L}(\boldsymbol{v}_1) &= \mathcal{L}(\rho^{\alpha_1}\boldsymbol{u}^{(1)}(\theta)) + \mathcal{L}(\hat{\boldsymbol{v}}_1) \\ &= \mathcal{L}(\hat{\boldsymbol{v}}_1) = 0 \quad \text{in } \Omega_\infty, \end{aligned} \tag{16}$$

$$\begin{aligned} \mathcal{T}(\boldsymbol{v}_1) &= \mathcal{T}(\rho^{\alpha_1}\boldsymbol{u}^{(1)}(\theta)) + \mathcal{T}(\hat{\boldsymbol{v}}_1) \\ &= \mathcal{T}(\hat{\boldsymbol{v}}_1) = 0 \quad \text{on } \Gamma_1, \Gamma_2, \end{aligned} \tag{17}$$

$$\begin{aligned} \mathcal{T}(\boldsymbol{v}_1) &= \mathcal{T}(\rho^{\alpha_1}\boldsymbol{u}^{(1)}(\theta)) + \mathcal{T}(\hat{\boldsymbol{v}}_1) \Rightarrow \mathcal{T}(\hat{\boldsymbol{v}}_1) \\ &= -\mathcal{T}(\rho^{\alpha_1}\boldsymbol{u}^{(1)}(\theta)) \quad \text{on } \Gamma_3, \Gamma_4, \end{aligned} \tag{18}$$

$$\boldsymbol{\sigma}(\hat{\boldsymbol{v}}_1) \underset{\rho\to\infty}{\sim} 0 \quad \text{or} \quad \hat{\boldsymbol{v}}_1 \underset{\rho\to\infty}{\sim} 0, \tag{19}$$

where $\mathcal{L}(\bullet)$ is the 2-D elasticity operator on the $\bullet$ displacements, $\mathcal{T}(\bullet) \stackrel{\text{def}}{=} \boldsymbol{\sigma}(\bullet)\cdot\boldsymbol{n}$ is the traction operator, and $\boldsymbol{\sigma}(\bullet)$ is the stress field. Notice, that α_1 and $\boldsymbol{u}^{(1)}$ are eigen-pairs of the V-notch problem so they satisfy identically the elasticity equations and traction free boundary conditions on the V-notch faces Γ_1, Γ_2.

Third term

Following similar arguments as for the second term one obtains: $d_2(\ell) = A_2\, \ell^{\alpha_2}$ and

$$\boldsymbol{v}_2(y_1,y_2) \sim \rho^{\alpha_2} \boldsymbol{u}^{(2)}(\theta) \quad \text{as } \rho \to \infty. \tag{20}$$

Furthermore,

$$\boldsymbol{v}_2(y_1,y_2) = \rho^{\alpha_2} \boldsymbol{u}^{(2)}(\theta) + \hat{\boldsymbol{v}}_2. \tag{21}$$

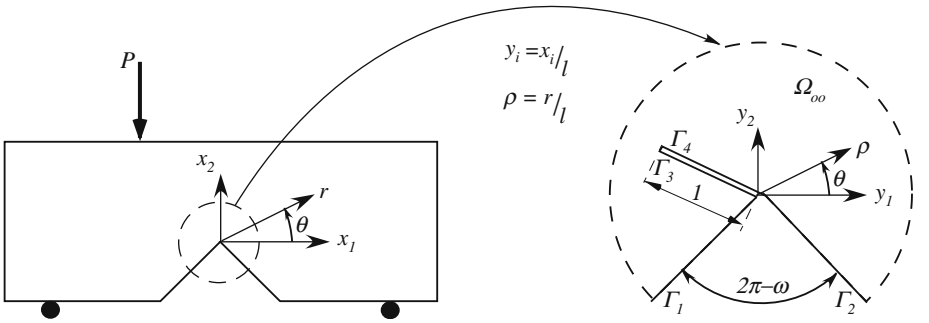

Fig. 5 Outer and inner expansions

where $\hat{\boldsymbol{v}}_2$ is the solution to the following elasticity problem:

$$\mathcal{L}(\hat{\boldsymbol{v}}_2) = 0 \quad \text{in } \Omega_\infty, \tag{22}$$

$$\mathcal{T}(\hat{\boldsymbol{v}}_2) = 0 \quad \text{on } \Gamma_1, \Gamma_2, \tag{23}$$

$$\mathcal{T}(\hat{\boldsymbol{v}}_2) = -\mathcal{T}(\rho^{\alpha_2}\boldsymbol{u}^{(2)}(\theta)) \quad \text{on } \Gamma_3, \Gamma_4, \tag{24}$$

$$\boldsymbol{\sigma}(\hat{\boldsymbol{v}}_2) \underset{\rho\to\infty}{\sim} 0 \quad \text{or} \quad \hat{\boldsymbol{v}}_2 \underset{\rho\to\infty}{\sim} 0. \tag{25}$$

Remark 1 In an unbounded domain traction free boundary conditions **are equivalent** to homogenous Dirichlet boundary conditions at infinity up to an irrelevant rigid motion.

Remark 2 It is more convenient to specify homogeneous Dirichlet boundary conditions at infinity than traction free boundary conditions to avoid the uncertainty on rigid motions.

Using the asymptotic analysis the expression for $\delta\Pi$ can be derived as follows.

3.2 Computing $\delta\Pi$

Consider the domain Ω_∞ in the vicinity of the crack at a V-notch tip, and a path Γ emanating at on face of the V-notch and terminating at the other face as shown in Fig. 6.

We define a path integral Ψ as following:

$$\Psi(\boldsymbol{f},\boldsymbol{g}) \overset{\text{def}}{=} \frac{1}{2}\int_\Gamma \left[\mathcal{T}(\boldsymbol{f})\boldsymbol{g} - \mathcal{T}(\boldsymbol{g})\boldsymbol{f}\right] \mathrm{d}S. \tag{26}$$

Using Betti's theorem one may show that:

$$\delta\Pi = \Pi(\ell) - \Pi(\ell = 0) = \Psi(\boldsymbol{u}_\ell, \boldsymbol{u}_0). \tag{27}$$

Substituting (13) and (12) in (27), and using the linearity property of the Ψ functional, one obtains:

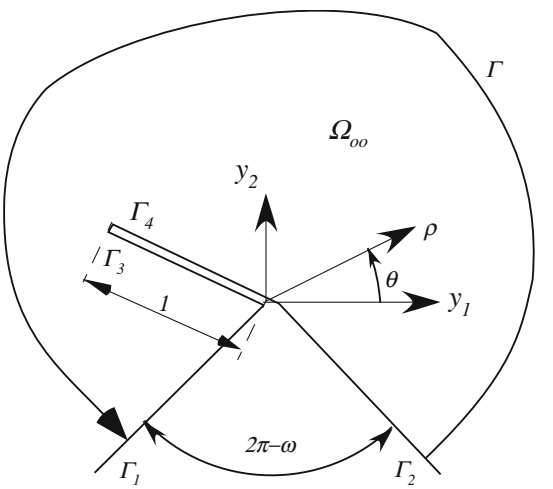

Fig. 6 The inner expansion infinite domain with a given path

$$\begin{aligned}
\delta\Pi = \Psi\big[&\left(\boldsymbol{u}(0,0) + A_1\ell^{\alpha_1}\left(\rho^{\alpha_1}\boldsymbol{u}^{(1)} + \hat{\boldsymbol{v}}_1\right)\right.\\
&+ \left. A_2\ell^{\alpha_2}\left(\rho^{\alpha_2}\boldsymbol{u}^{(2)} + \hat{\boldsymbol{v}}_2\right)\right)\left(\boldsymbol{u}(0,0)\right.\\
&+ \left. A_1\ell^{\alpha_1}\rho^{\alpha_1}\boldsymbol{u}^{(1)} + A_2\ell^{\alpha_2}\rho^{\alpha_2}\boldsymbol{u}^{(2)}\right)\big] + h.o.t.\\
= \Psi(\boldsymbol{u}(0,0), &\boldsymbol{u}(0,0)) + A_1\ell^{\alpha_1}\Psi(\boldsymbol{u}(0,0), \rho^{\alpha_1}\boldsymbol{u}^{(1)})\\
&+ A_2\ell^{\alpha_2}\Psi(\boldsymbol{u}(0,0), \rho^{\alpha_2}\boldsymbol{u}^{(2)})\\
&+ A_1\ell^{\alpha_1}\Psi(\rho^{\alpha_1}\boldsymbol{u}^{(1)} + \hat{\boldsymbol{v}}_1, \boldsymbol{u}(0,0))\\
&+ A_1^2\ell^{2\alpha_1}\Psi(\rho^{\alpha_1}\boldsymbol{u}^{(1)} + \hat{\boldsymbol{v}}_1, \rho^{\alpha_1}\boldsymbol{u}^{(1)})\\
&+ A_1A_2\ell^{\alpha_1+\alpha_2}\Psi(\rho^{\alpha_1}\boldsymbol{u}^{(1)} + \hat{\boldsymbol{v}}_1, \rho^{\alpha_2}\boldsymbol{u}^{(2)})\\
&+ A_2\ell^{\alpha_2}\Psi(\rho^{\alpha_2}\boldsymbol{u}^{(2)} + \hat{\boldsymbol{v}}_2, \boldsymbol{u}(0,0))\\
&+ A_2A_1\ell^{\alpha_1+\alpha_2}\Psi(\rho^{\alpha_2}\boldsymbol{u}^{(2)} + \hat{\boldsymbol{v}}_2, \rho^{\alpha_1}\boldsymbol{u}^{(1)})\\
&+ A_2^2\ell^{2\alpha_2}\Psi(\rho^{\alpha_2}\boldsymbol{u}^{(2)} + \hat{\boldsymbol{v}}_2, \rho^{\alpha_2}\boldsymbol{u}^{(2)}) + h.o.t.
\end{aligned} \tag{28}$$

By definition $\Psi(\boldsymbol{f},\boldsymbol{f}) = 0$, and because distinct eigen-pairs are bi-orthogonal under the Ψ-integral, i.e. $\Psi(\boldsymbol{u}^{(i)}, \boldsymbol{u}^{(j)}) = 0$ if $i \neq -j$ (see Blum and

Dobrowolski 1982), then (28) reduces to:

$$\begin{aligned}\delta\Pi = {} & A_1\ell^{\alpha_1}\Psi(\boldsymbol{u}(0,0),\rho^{\alpha_1}\boldsymbol{u}^{(1)})+A_2\ell^{\alpha_2}\Psi(\boldsymbol{u}_0,\rho^{\alpha_2}\boldsymbol{u}^{(2)})\\ & + A_1\ell^{\alpha_1}\Psi(\rho^{\alpha_1}\boldsymbol{u}^{(1)}+\hat{\boldsymbol{v}}_1,\boldsymbol{u}(0,0))\\ & + A_1^2\ell^{2\alpha_1}\Psi(\hat{\boldsymbol{v}}_1,\rho^{\alpha_1}\boldsymbol{u}^{(1)})\\ & + A_1A_2\ell^{\alpha_1+\alpha_2}\Psi(\hat{\boldsymbol{v}}_1\,,\rho^{\alpha_2}\boldsymbol{u}^{(2)})\\ & + A_2\ell^{\alpha_2}\Psi(\rho^{\alpha_2}\boldsymbol{u}^{(2)}+\hat{\boldsymbol{v}}_2\,,\boldsymbol{u}(0,0))\\ & + A_2A_1\ell^{\alpha_1+\alpha_2}\Psi(\hat{\boldsymbol{v}}_2\,,\rho^{\alpha_1}\boldsymbol{u}^{(1)})\\ & + A_2^2\ell^{2\alpha_2}\Psi(\hat{\boldsymbol{v}}_2\,,\rho^{\alpha_2}\boldsymbol{u}^{(2)})+h.o.t. \end{aligned} \tag{29}$$

Another observation is that $\boldsymbol{u}(0,0)$ is a constant vector, therefore $\mathcal{T}(\boldsymbol{u}(0,0))=0$ and expressions like $\Psi(\boldsymbol{u}(0,0),\rho^{\alpha_i}\boldsymbol{u}^{(i)})$ become:

$$\begin{aligned}&\Psi(\boldsymbol{u}(0,0),\rho^{\alpha_i}\boldsymbol{u}^{(i)})\\ &\quad=\frac{1}{2}\int_\Gamma\Big[\mathcal{T}(\boldsymbol{u}(0,0))\rho^{\alpha_i}\boldsymbol{u}^{(i)}-\mathcal{T}(\rho^{\alpha_i}\boldsymbol{u}^{(i)})\boldsymbol{u}(0,0)\Big]\,\mathrm{d}S,\\ &\quad=-\frac{\boldsymbol{u}_0}{2}\int_\Gamma\mathcal{T}(\rho^{\alpha_i}\boldsymbol{u}^{(i)})\mathrm{d}S. \end{aligned} \tag{30}$$

Furthermore, because $\mathcal{T}(\rho^{\alpha_i}\boldsymbol{u}^{(i)})$ is the traction associated with an eigen-pair, and because the V-notch faces are free of tractions, (and the integrals along Γ_3 and Γ_4 cancel as they are along same line in opposite directions) one may use the Green theorem to transform the path integral into an area integral in which the elasticity operator acts on the eigen-pair, obtaining:

$$\Psi(\boldsymbol{u}(0,0),\rho^{\alpha_i}\boldsymbol{u}^{(i)})=-\frac{\boldsymbol{u}(0,0)}{2}\int_{\Omega_\infty}\mathcal{L}(\rho^{\alpha_i}\boldsymbol{u}^{(i)})\mathrm{d}\Omega.$$

Because the eigen-pairs identically satisfy the homogeneous elasticity operator then $\Psi(\boldsymbol{u}(0,0),\rho^{\alpha_i}\boldsymbol{u}^{(i)})=0$, simplifying (29) to:

$$\begin{aligned}\delta\Pi = {} & A_1\ell^{\alpha_1}\Psi(\hat{\boldsymbol{v}}_1\,,\boldsymbol{u}(0,0))+A_1^2\ell^{2\alpha_1}\Psi(\hat{\boldsymbol{v}}_1\,,\rho^{\alpha_1}\boldsymbol{u}^{(1)})\\ & + A_1A_2\ell^{\alpha_1+\alpha_2}\Psi(\hat{\boldsymbol{v}}_1\,,\rho^{\alpha_2}\boldsymbol{u}^{(2)})\\ & + A_2\ell^{\alpha_2}\Psi(\hat{\boldsymbol{v}}_2\,,\boldsymbol{u}(0,0))\\ & + A_2A_1\ell^{\alpha_1+\alpha_2}\Psi(\hat{\boldsymbol{v}}_2\,,\rho^{\alpha_1}\boldsymbol{u}^{(1)})\\ & + A_2^2\ell^{2\alpha_2}\Psi(\hat{\boldsymbol{v}}_2\,,\rho^{\alpha_2}\boldsymbol{u}^{(2)})+h.o.t. \end{aligned} \tag{31}$$

One may also show that $\Psi(\hat{\boldsymbol{v}}_i\,,\boldsymbol{u}(0,0))=0$ as follows. Because $\boldsymbol{u}(0,0)$ is constant:

$$\Psi(\hat{\boldsymbol{v}}_i\,,\boldsymbol{u}(0,0))=\frac{\boldsymbol{u}_0}{2}\int_\Gamma\mathcal{T}(\hat{\boldsymbol{v}}_i)\,\mathrm{d}S.$$

Again, due to the V-notch traction free faces $\mathcal{T}(\hat{\boldsymbol{v}}_i)=0$ on Γ_1 and Γ_2, (and the integrals along Γ_3 and Γ_4 cancel as they are along same line in opposite directions) one may use the Green theorem to transform the path integral into an area integral, obtaining:

$$\Psi(\hat{\boldsymbol{v}}_i\,,\boldsymbol{u}(0,0))=\frac{\boldsymbol{u}_0}{2}\int_{\Omega_\infty}\mathcal{L}(\hat{\boldsymbol{v}}_i)\mathrm{d}\Omega=0.$$

Thus, (31) becomes:

$$\begin{aligned}\delta\Pi = {} & A_1^2\ell^{2\alpha_1}\Psi(\hat{\boldsymbol{v}}_1\,,\rho^{\alpha_1}\boldsymbol{u}^{(1)})\\ & + A_1A_2\ell^{\alpha_1+\alpha_2}\Big[\Psi(\hat{\boldsymbol{v}}_1,\rho^{\alpha_2}\boldsymbol{u}^{(2)})+\Psi(\hat{\boldsymbol{v}}_2,\rho^{\alpha_1}\boldsymbol{u}^{(1)})\Big]\\ & + A_2^2\ell^{2\alpha_2}\Psi(\hat{\boldsymbol{v}}_2\,,\rho^{\alpha_2}\boldsymbol{u}^{(2)})+h.o.t. \end{aligned} \tag{32}$$

Introducing the definition of the geometrical parameters:

$$\begin{aligned}&-\Psi(\hat{\boldsymbol{v}}_i\,,\rho^{\alpha_i}\boldsymbol{u}^{(i)})\overset{\text{def}}{=}H_{ii},\\ &-\Psi(\hat{\boldsymbol{v}}_i\,,\rho^{\alpha_j}\boldsymbol{u}^{(j)})\overset{\text{def}}{=}H_{ij},\\ &-\Psi(\hat{\boldsymbol{v}}_j\,,\rho^{\alpha_i}\boldsymbol{u}^{(i)})\overset{\text{def}}{=}H_{ji} \end{aligned} \tag{33}$$

the expression in (32) becomes:

$$\begin{aligned}-\delta\Pi = {} & A_1^2\ell^{2\alpha_1}H_{11}+A_1A_2\ell^{\alpha_1+\alpha_2}(H_{12}+H_{21})\\ & + A_2^2\ell^{2\alpha_2}H_{22}+h.o.t, \end{aligned} \tag{34}$$

which is precisely (9).

Remark 3 The geometrical parameters H_{ij}, per definition, depend only on the material properties, V-notch solid angle ω and direction of crack initiation θ_0, and are independent of the loading or crack length provided the crack length remains small compared to the specimen size (asymptotic assumption).

The asymptotic expression of $\delta\Pi$ is used in the toughness criterion so to formulate the failure criterion for mixed mode loading.

3.3 Failure criterion for mixed mode loading

Substituting (9) into the toughness criterion (7) one obtains the lower limit for ℓ:

$$\begin{aligned}&A_1^2\ell^{2\alpha_1-1}H_{11}(\omega,\theta_0)+A_1A_2\ell^{\alpha_1+\alpha_2-1}(H_{12}(\omega,\theta_0)\\ &\quad+H_{21}(\omega,\theta_0))+A_2^2\ell^{2\alpha_2-1}H_{22}(\omega,\theta_0)\geq G_{\mathrm{c}}. \end{aligned} \tag{35}$$

On the other hand, the upper limit for ℓ is the maximum distance from the V-notch tip at an angle θ_0 at which the tangential stress is higher than σ_{c} (strength criterion):

$$\sigma_{\theta\theta}(\ell,\theta_0)=A_1\ell^{\alpha_1-1}\sigma_{\theta\theta}^{(1)}(\theta_0)+A_2\ell^{\alpha_2-1}\sigma_{\theta\theta}^{(2)}(\theta_0)\geq\sigma_{\rm c}. \tag{36}$$

For $\frac{1}{2}\leq\alpha_1\leq\alpha_2\leq 1$, the exponents of ℓ in (35) are positive, whereas in (36) are negative. Defining:

$$m(\ell)\stackrel{\rm def}{=}\frac{A_2}{A_1}\ell^{\alpha_2-\alpha_1}, \tag{37}$$

we may reformulates (35) and (36):

$$\ell\geq\left(\frac{G_{\rm c}}{A_1^2\left[H_{11}(\omega,\theta_0)+m(H_{12}(\omega,\theta_0)+H_{21}(\omega,\theta_0))+m^2H_{22}(\omega,\theta_0)\right]}\right)^{1/2\alpha_1-1}, \tag{38}$$

$$\ell\leq\left(\frac{A_1(\sigma_{\theta\theta}^{(1)}(\theta_0)+m\sigma_{\theta\theta}^{(2)}(\theta_0))}{\sigma_{\rm c}}\right)^{2/2-2\alpha_1}. \tag{39}$$

If both the toughness and strength criteria have to hold at the instance of crack jump then the lower and upper bound of ℓ in (38) and (38) have to coincide. This results in the following generalized stress intensity factor:

$$A_1^{-2}=\left(\frac{G_{\rm c}}{H_{11}(\omega,\theta_0)+m(H_{12}(\omega,\theta_0)+H_{21}(\omega,\theta_0))+m^2H_{22}(\omega,\theta_0)}\right)^{-2+2\alpha_1}\times\left(\frac{(\sigma_{\theta\theta}^{(1)}(\theta_0)+m\sigma_{\theta\theta}^{(2)}(\theta_0))^2}{\sigma_{\rm c}^2}\right)^{2\alpha_1-1}. \tag{40}$$

Substituting (38), one obtains the finite crack size ℓ_0 that has to be generated instantly so to satisfy (35 and 36) simultaneously:

$$\ell_0=\frac{G_{\rm c}}{H_{11}(\omega,\theta_0)+m(\ell_0)(H_{12}(\omega,\theta_0)+H_{21}(\omega,\theta_0))+m^2(\ell_0)H_{22}(\omega,\theta_0)}\times\left(\frac{\sigma_{\theta\theta}^{(1)}(\theta_0)+m(\ell_0)\sigma_{\theta\theta}^{(2)}(\theta_0)}{\sigma_{\rm c}}\right)^2. \tag{41}$$

Note, that the determination of ℓ_0 requires a solution of an implicit equation because m depends on ℓ_0.

After ℓ_0 is determined, $m(\ell_0)$ is known and can be substituted in (38) to obtain the GSIF at failure, denoted by $A_{1\rm c}$:

$$A_{1\rm c}=\left(\frac{G_{\rm c}}{H_{11}(\omega,\theta_0)+m(H_{12}(\omega,\theta_0)+H_{21}(\omega,\theta_0))+m^2H_{22}(\omega,\theta_0)}\right)^{\alpha_1-1}\times\left(\frac{\sigma_{\rm c}}{\sigma_{\theta\theta}^{(1)}(\theta_0)+m\sigma_{\theta\theta}^{(2)}(\theta_0)}\right)^{2\alpha_1-1}. \tag{42}$$

Remark 4 Notice that $A_{1\rm c}$ depends on θ_0 and the mode mixity ratio A_2/A_1. This means that for each θ_0 a different value of $A_{1\rm c}$ is obtained. Therefore, the angle θ_0 that produces the smallest value of $A_{1\rm c}$ for a given A_2/A_1 is the crack initiation angle and is denoted by $\theta_{0\rm c}$.

Notice, that ℓ_0 depends on θ_0 also. Therefore for the determination of the critical GSIF one has to determine ℓ_0 for all values of θ_0, and use these ℓ_0 for each angle to determine the minimum value of $A_{1\rm c}$.

Under mode I loading, for which $A_2=0$, (38) degenerates to the explicit expression (28) in Leguillon (2002).

4 Computing the ingredients required for the failure criterion

The failure criterion (38) requires the determination of H_{ij}-values, therefore the $\hat{\boldsymbol{v}}_i$ displacements have to be computed by numerical methods in an

infinite domain, followed by a path integral to be chosen. These geometrical functions need to be computed for any ω and θ_0 once only and used thereafter.

4.1 Computation of H_{ij} functions

In practical application we choose a finite circular domain having a large radius $R \gg 1$, and solve (16–18) and (22–25) on this domain. The outer circular surface of the domain is used as the path over, which H_{ij}s are computed. On the circular domain $\hat{\boldsymbol{v}}_i = 0$ therefore (33) is simplified:

$$H_{ii} = -\Psi\left(\hat{\boldsymbol{v}}_i\,, \rho^{\alpha_i}\boldsymbol{u}^{(i)}\right) = -\frac{1}{2}\int_{-\pi/2+\omega/2}^{3\pi/2-\omega/2} \times \mathcal{T}(\hat{\boldsymbol{v}}_i)\big|_R\, R^{\alpha_i}\boldsymbol{u}^{(i)} R\,\mathrm{d}\theta = -\frac{R^{\alpha_i+1}}{2}\int_{-\pi/2+\omega/2}^{3\pi/2-\omega/2} \times \mathcal{T}(\hat{\boldsymbol{v}}_i)\big|_R\, \boldsymbol{u}^{(i)}(\theta)\,\mathrm{d}\theta, \tag{43}$$

$$H_{ij} + H_{ji} = -\Psi\left(\hat{\boldsymbol{v}}_i\,, \rho^{\alpha_j}\boldsymbol{u}^{(j)}\right) - \Psi\left(\hat{\boldsymbol{v}}_j\,, \rho^{\alpha_i}\boldsymbol{u}^{(i)}\right) = -\frac{R^{\alpha_j+1}}{2}\int_{-\pi/2+\omega/2}^{3\pi/2-\omega/2} \mathcal{T}(\hat{\boldsymbol{v}}_i)\big|_R\, \boldsymbol{u}^{(j)}(\theta)\,\mathrm{d}\theta - \frac{R^{\alpha_i+1}}{2}\int_{-\pi/2+\omega/2}^{3\pi/2-\omega/2} \mathcal{T}(\hat{\boldsymbol{v}}_j)\big|_R\, \boldsymbol{u}^{(i)}(\theta)\,\mathrm{d}\theta \quad ; i \neq j. \tag{44}$$

The algorithm for the computation of the H_{ij} functions using finite element methods is as follows:

1. For a given V-notch solid angle, ω, determine analytically the eigen-pairs α_i and $\boldsymbol{u}^{(i)}(\theta)$ for $i = 1, 2$, according to Sect. 2.
2. Create a finite element model of a circular sector of radius R (as a parameter) having a V-notch of an opening angle solid ω with a crack of length 1 at its tip at an angle θ_0.
3. Homogeneous Dirichlet boundary conditions are applied on the outer perimeter of the sector at $\rho = R$ and traction free BCs on the V-notch faces.
4. On the crack faces *two* different sets of tractions are applied:
$$\sigma_{\theta\theta}(\theta_0) = -\sigma_{\theta\theta}\left(\rho^{\alpha_1}\boldsymbol{u}^{(1)}(\theta_0)\right), \tag{45}$$
$$\sigma_{r\theta}(\theta_0) = -\sigma_{r\theta}\left(\rho^{\alpha_1}\boldsymbol{u}^{(1)}(\theta_0)\right), \tag{46}$$
$$\sigma_{\theta\theta}(\theta_0) = -\sigma_{\theta\theta}\left(\rho^{\alpha_2}\boldsymbol{u}^{(2)}(\theta_0)\right), \tag{47}$$
$$\sigma_{r\theta}(\theta_0) = -\sigma_{r\theta}\left(\rho^{\alpha_2}\boldsymbol{u}^{(2)}(\theta_0)\right). \tag{48}$$
5. Two finite element solutions for each set of tractions are obtained: $\hat{\boldsymbol{v}}_1$ and $\hat{\boldsymbol{v}}_2$, on a domain having an outer radius $R = 200$. We have verified that $\hat{\boldsymbol{v}}_i$ are unaffected by the outer radius when increasing it to $R = 300, 400, 500$. Also, the FE numerical errors were below 1.5% in energy norm.
6. The final step is computation of (44) and (44) at the path $\rho = R$ for $i, j = 1, 2$ using Gaussian quadrature of high-order (90 Gaussian points) to ensure an accuracy of numerical integration.
7. Return to Step 2 with a different angle θ_0 of the crack.

4.1.1 The finite element model

We create a 2-D, plane-strain FE model consisting of a circular section with a solid angle ω with a crack of length 1 using the *p*-version FE code StressCheck.[1] As an example, a model with a crack at an angle of $\theta_0 = 80°$ at a $\omega = 315°$ V-notch tip is shown in Fig. 7. The crack inclination angle θ_0 and V-notch solid angle ω may be changed parametrically. We perform FE analyses increasing the polynomial order from $p = 1$ to $p = 8$ and monitor the relative error in energy norm so it is below 1.5% for all FE analyses reported in the sequel.

The outer radius was taken to be $R = 200$ and to ensure that the model simulates the unbounded domain, computations were also preformed for $R = 300, 400$ and 500. It was found that in this range R has negligible influence on the H_{ij} values.

Homogeneous Dirichlet boundary conditions are prescribed over the outer perimeter ($u_r = u_\theta = 0$) whereas the V-notch faces are traction free. On the crack faces the traction boundary conditions (45–48) are prescribed as shown in Fig. 8.

Denoting the stresses obtained by the FEA when BCs (45 and 46) are applied on the crack face by the superscript $\sigma^{(\mathrm{FE}-1)}$, and the ones obtained when BCs (47 and 48) are applied by $\sigma^{(\mathrm{FE}-2)}$, we can compute H_{11}, H_{22}, H_{12} numerically using

[1] StressCheck is a trademark of Engineering Software Research and Development, Inc., St. Louis, MO, USA.

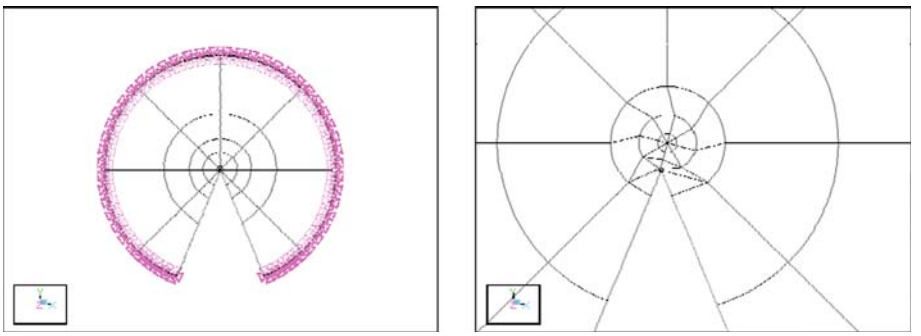

Fig. 7 p-FE model for H_{ij} extraction. *Left* The FE model, *Right* Zoom at the crack at the V-notch tip

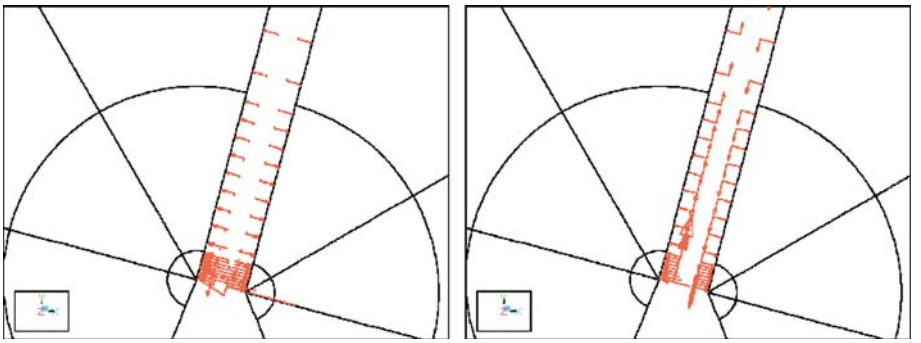

Fig. 8 Traction applied on the crack edges: *Left* mode I, *Right* mode II

Gaussian quadrature:

$$H_{11} = \frac{R^{\alpha_1+1}}{2}\frac{\omega}{2}\sum_{i=1}^{N} W_i\Big(\sigma_{rr}^{(\mathrm{FE}-1)}(\theta_i)u_r^{(1)}(\theta_i) + \sigma_{r\theta}^{(\mathrm{FE}-1)}(\theta_i)u_\theta^{(1)}(\theta_i)\Big)_{r=R,} \tag{49}$$

$$H_{22} = \frac{R^{\alpha_2+1}}{2}\frac{\omega}{2}\sum_{i=1}^{N} W_i\Big(\sigma_{rr}^{(\mathrm{FE}-2)}(\theta_i)u_r^{(2)}(\theta_i) + \sigma_{r\theta}^{(\mathrm{FE}-2)}(\theta_i)u_\theta^{(2)}(\theta_i)\Big)_{r=R,} \tag{50}$$

$$\begin{aligned} H_{12}+H_{21} = {} & \frac{R^{\alpha_2+1}}{2}\frac{\omega}{2}\sum_{i=1}^{N} W_i\Big(\sigma_{rr}^{(\mathrm{FE}-1)}(\theta_i)u_r^{(2)}(\theta_i) \\ & + \sigma_{r\theta}^{(\mathrm{FE}-1)}(\theta_i)u_\theta^{(2)}(\theta_i)\Big)_{r=R,} \\ & + \frac{R^{\alpha_1+1}}{2}\frac{\omega}{2}\sum_{i=1}^{N} W_i\Big(\sigma_{rr}^{(\mathrm{FE}-2)}(\theta_i)u_r^{(1)}(\theta_i) \\ & + \sigma_{r\theta}^{(\mathrm{FE}-2)}(\theta_i)u_\theta^{(1)}(\theta_i)\Big)_{r=R,} \end{aligned} \tag{51}$$

Were N is the Gaussian quadrature order, W_i are the Gaussian weights, and θ_i are the angles associated with the abcissas or the Gaussian quadrature.

4.1.2 Results

For a material with Young modulus $E = 1$ (MPa) and Poisson ratio $\nu = 0.36$ we computed the functions H_1, H_2, H_{12} for $\omega = 330°, 315°, 300°, 270°$, and 240° for crack angles ranging from $\theta = 30°$–$\theta = 150°$. H_{ij} functions for any other E in (MPa) and ν can be easily obtained by

$$H_{ij}^{\mathrm{new}}(\omega,\theta_0) = H_{ij}(\omega,\theta_0)\frac{1}{1-0.36^2}\frac{1-\nu^2}{E}. \tag{52}$$

In order to demonstrate the convergence of H_{ij}, we present in Table 2 the values obtained at $p = 6, 7, 8$ for $\omega = 315°$ and $\theta_0 = 79.5$.

The effect on domain's outer radius R on the results is demonstrated by computing H_{ij} at various R =100–400, as shown in Table 3.

In Tables 4 and 5, we summarize H_{ij} for $E = 1$ (MPa) and $\nu = 0.36$ and $\omega = 330°, 315°,$

Table 2 H_{ij} for $\omega = 315°$ and $\theta_0 = 79.5$ at different p-FE levels $E = 1$ MPa, $\nu = 0.36$

FE p-level	H_{ij} values		
	H_{11}	H_{22}	$H_{12} + H_{21}$
6	5.2408	3.2242	1.671
7	5.2420	3.2208	1.669
8	5.2433	3.2237	1.670

Table 3 H_{ij} for $\omega = 315°$ and $\theta_0 = 79.5$ on domains with different Rs ($E = 1$ MPa, $\nu = 0.36$)

R	H_{ij} values		
	H_{11}	H_{22}	$H_{12} + H_{21}$
100	5.219	3.221	1.660
200	5.243	3.224	1.670
300	5.251	3.224	1.672
400	5.255	3.224	1.674

$300°, 270°, 240°$, also plotted in Fig. 9. Only the angles θ_0 from 30 to 90° are provided in the tables because:

$$H_{ii}(\theta = 90 - \beta) = H_{ii}(\theta = 90 + \beta),$$
$$H_{ij}(\theta = 90 - \beta) = -H_{ij}(\theta = 90 + \beta).$$

4.2 Verification of the asymptotic expression for $\delta\Pi$

After computing the geometrical functions $H_{ij}(\omega, \theta)$ we verify that (9) holds true. We consider a V-notched specimen with $\omega = 315°$ and assume a crack of length $\ell = 0.01$ initiates at an angle $\theta_0 = 80°$ at the V-notch tip. The specimen's dimensions and finite element mesh used are shown in Fig. 10. The specimen is loaded by a non-symmetric three point bending load $P = 1$ [N]. Assume the specimen is made of PMMA having $E = 3100$(Mpa) and $\nu = 0.36$, then, we can compute $-\delta\Pi$ by two different FE analyses of the V-notched specimen with and without the crack. Using the mesh shown in Fig. 10, we obtained $-\delta\Pi^{\mathrm{FE}} = 3.322 \times 10^{-7}$ with a numerical error in energy norm of less than 1%. On the other hand, for the V-notch in PMMA, we obtain $H_{11} = 0.00169$, $H_{22} = 0.00103$, and $H_{12} + H_{21} = 0.00051$, and for the shown a-symmetric loading we have $A_1 = 0.0446\,\mathrm{MPa\ mm}^{1-\alpha_1}$ for a unit load and $A_2/A_1 = 0.217mm - 0.135$, $m = 0.105$, so we may use (9) to compute $-\delta\Pi = 3.350 \times 10^{-7}$. The obtained value is less than 1% difference compared to the finite element solution. For a larger crack length $\ell = 0.05$, $m = 0.135$ and, we obtain $-\delta\Pi^{\mathrm{FE}} = 1.7018 \times 10^{-6}$ and $-\delta\Pi = 1.7246 \times 10^{-6}$, having a relative difference of about 1.5%.

5 Validation of the failure criterion by experimental observation

We validate the failure criterion presented herein by comparing the predicted loads at failure and crack initiation angles to these obtained by experimental observations. We consider experiments on PMMA specimens having different V-notch angles and mode mixity ratios reported in Seweryn and Lukaszewicz (2002), as well as experiments performed on specimens made of PMMA and Macor (machinable ceramics) having a 315° V-notch for different mode mixity ratios.

5.1 Experiments on PMMA reported

In Seweryn and Lukaszewicz (2002) several experiments preformed on double V-notched PMMA specimens at room temperature with different notch opening angles are reported. The material parameters reported in Seweryn and Lukaszewicz (2002) for PMMA are $E = 3300\,\mathrm{MPa}$, $\nu = 0.35$, $K_{\mathrm{Ic}} = 1.202\,\mathrm{MPa}\sqrt{m}$, $\sigma_{\mathrm{c}} = 102.8\,\mathrm{MPa}$, and specimens were loaded so to produce mixed mode loading. In order to predict the critical load using the proposed failure criterion the mode mixity A_2/A_1 is required. Because, the applied boundary conditions in the reported experiments are not well understood, we extract the values of the force at failure F_{c} as reported in the graphs for each loading angle φ. These values are used to compute the normal P and tangential T components of the force at failure $P = F_{\mathrm{c}} \times \cos(\varphi)$ and $T = F_{\mathrm{c}} \times \sin(\varphi)$. Finally, the stress intensity factors at failure can be obtained from Table 1 in Seweryn and Lukaszewicz (2002) where the values of ξ_{I} and ξ_{II} are reported for different V-notch opening angles.

For example, we provide the method for computing the ratio A_2/A_1 for $\omega = 320°$ ($\alpha_1 = 0.503, \alpha_2 = 0.638$) for the specimen loaded at $\varphi = 30°$. We retrieve from Table 1 in Seweryn and

Table 4 H_{ij} for $\omega = 315°, 330°, 300°$ ($E = 1$ MPa, $\nu = 0.36$)

θ_0	$\omega = 330°$			$\omega = 315°$			$\omega = 300°$		
	H_{11}	H_{22}	$H_{12}+H_{21}$	H_{11}	H_{22}	$H_{12}+H_{21}$	H_{11}	H_{22}	$H_{12}+H_{21}$
30°	3.0965	5.5913	6.3403	3.0600	4.6212	5.8688	2.9552	3.8332	5.4388
35°	3.3952	5.4651	6.2988	3.3566	4.5299	5.8488	3.2627	3.7196	5.3466
40°	3.6885	5.3045	6.1559	3.6476	4.4054	5.7318	3.5502	3.6272	5.2614
45°	3.9718	5.1185	5.9101	3.9283	4.2551	5.5158	3.8272	3.5085	5.0809
50°	4.2404	4.9168	5.5623	4.1941	4.0878	5.2013	4.0893	3.3713	4.8056
55°	4.4899	4.7095	5.1159	4.4204	3.9126	4.7917	4.3320	3.2242	4.4384
60°	4.7160	4.5062	4.5770	4.6634	3.7380	4.2840	4.5515	3.0756	3.9847
65°	4.9146	4.3163	3.9539	4.8591	3.5741	3.7161	4.7439	2.9337	3.4519
70°	5.0822	4.1482	3.2571	5.0243	3.4282	3.0544	4.9061	2.8061	2.8499
75°	5.2159	4.0094	2.4988	5.1552	3.3076	2.3443	5.0352	2.6994	2.1902
80°	5.3132	3.9058	1.6930	5.2510	3.2161	1.5881	5.1291	2.6192	1.4858
85°	5.3722	3.8418	0.8550	5.3096	3.1502	0.8003	5.1860	2.5694	0.7509
90°	5.3920	3.8202	5.614E-04	5.3287	3.1409	6.753E-04	5.2051	2.5525	7.06E-04

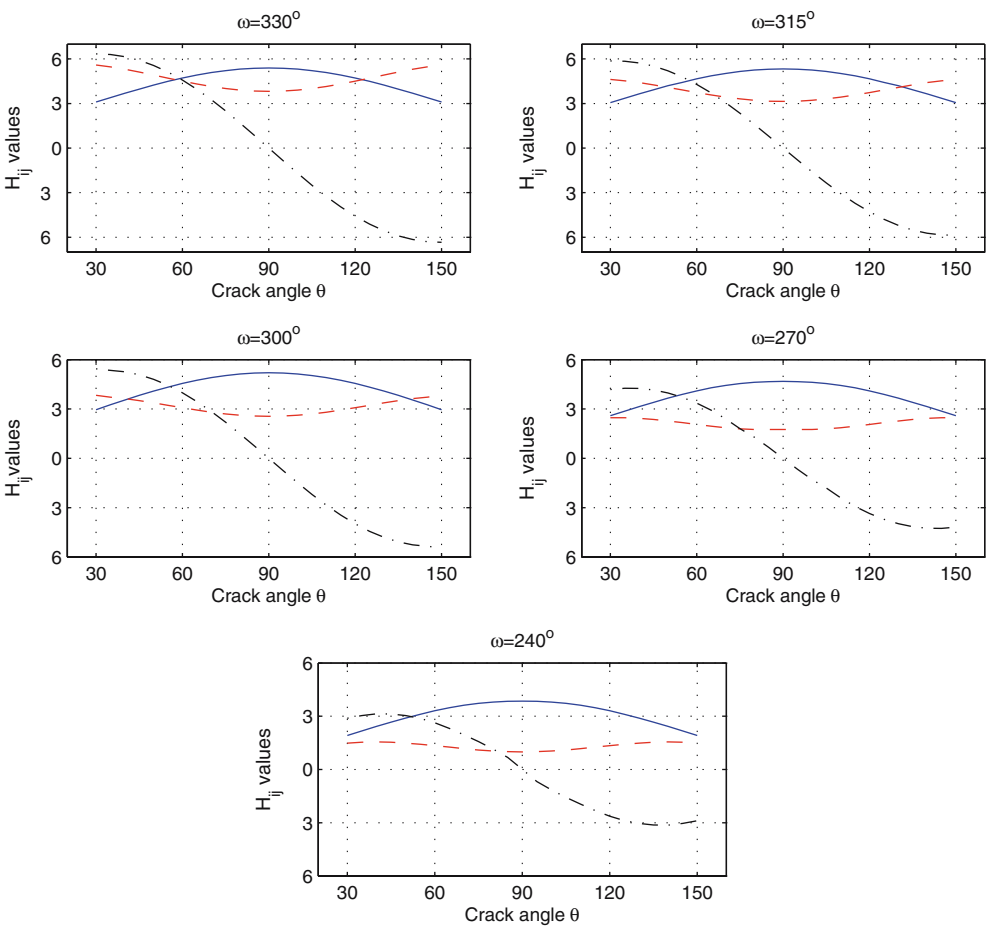

Fig. 9 H_{ij} for $\omega = 315°$ ($E = 1$ (MPa) and $\nu = 0.36$) for $\omega = 330°, 315°, 300°, 270°, 240°$. *Solid line* H_{11}, *Dashed line* H_{22}, *Dotted line* $H_{12} + H_{21}$

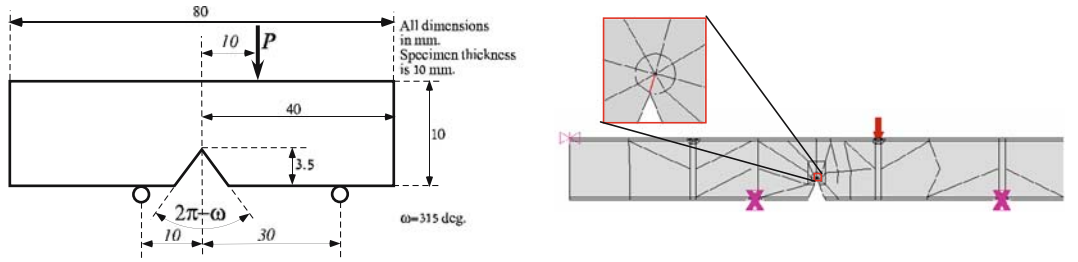

Fig. 10 PMMA specimen with a V-notch and the finite element mesh

Lukaszewicz (2002) $\xi_{\mathrm{I}} = 0.6323$ and $\xi_{\mathrm{II}} = 0.9981$ and from Fig. 15 in Seweryn and Lukaszewicz (2002) we obtain $F_{\mathrm{c}}/P_{\mathrm{c}} \approx 1.11$ for $\varphi = 30°$ (the average value of three experimental points). The value of P_{c} (critical load for pure tensile loading of the relevant V-notch opening angle) is reported in Fig. 13 in Seweryn and Lukaszewicz (2002), $P_{\mathrm{c}} = 1.954$ kN, therefore, we may compute $F_{\mathrm{c}} = 1.11 \times 1.954 = 2.150$ kN. The next step is computing $P = F_{\mathrm{c}} \times \cos(\varphi) = 1.861$ kN and $T = F_{\mathrm{c}} \times \sin(\varphi) = 1.075$ kN. Finally, using ξ_{I} and ξ_{II}, we may compute the so-called stress intensity factors in Seweryn and Lukaszewicz (2002) $K_{\mathrm{I}} = 1.17\,\mathrm{MPa\ m}^{0.497}$ and $K_{\mathrm{II}} = 1.07\,\mathrm{MPa\ m}^{0.362}$. Because, we use a unit system of MPa and mm, then after a unit transformation $K_{\mathrm{I}} = 36.343\,\mathrm{MPa\ mm}^{0.497}$ and $K_{\mathrm{II}} = 13.062\,\mathrm{MPa\ mm}^{0.362}$, i.e. $K_{\mathrm{II}}/K_{\mathrm{I}} = 0.359\,\mathrm{mm}^{-0.135}$. Notice, that the GSIFs used in our analysis do not include the 2π factor as the stress intensity factors in Seweryn and Lukaszewicz (2002), therefore $K_{\mathrm{II}}/K_{\mathrm{I}}$ has to be multiplied by $\frac{(2\pi)^{0.497}}{(2\pi)^{0.362}}$ to finally obtain $A_2/A_1 = 0.460\,\mathrm{mm}^{-0.135}$.

For the given V-notch angle and for all possible crack initiation angles, the values of H_{ij} are computed according to Sect. 4 and the values of ℓ_0 and $A_{1\mathrm{c}}$ are computed by (38) and (38) for the given notch angle and mode mixity. We preform the calculations for different crack initiation angles ranging from $\theta = 30$–$\theta = 90°$. The crack initiation angle is determined by the angle that provides the lowest value of $A_{1\mathrm{c}}$.

The value of $A_{1\mathrm{c}}$ is compared to the value of A_1 computed according to K_{I} at failure. For our example problem we compute $A_{1\mathrm{c}}^{(\mathrm{min})} = 0.453\,\mathrm{MPa\ m}^{0.497}$ at $\theta_{\mathrm{c}} = 65°$ compared to the experimental critical value of $A_{1\mathrm{c}} = 0.460\,\mathrm{MPa\ m}^{0.497}$ and $\theta_{\mathrm{c}} \approx 65°$. This gives as a critical load prediction of $F_{\mathrm{c}} = 2118$ N in comparison to the average experimental critical load of 2150 N.

In Tables 6 and 7, we summarize the experimental results for two V-notch opening angles from Seweryn and Lukaszewicz (2002), and the predicted values by the presented failure criterion.

The failure loads in three experiments reported in Seweryn and Lukaszewicz (2002) for the two V-notch angles 320 and 280° for different load mixity ratios is compared to the predicted failure load in Fig. 11, and the crack initiation angle in experiments compared to the one predicted is shown in Fig. 12.

One may notice the very good predictability of the failure load and crack initiation angle for the $\omega = 320°$ specimens for all mode mixity values. For the specimens with a V-notch angle of $\omega = 280°$ the failure load is predicted well for a mixity ratio until $A_2/A_1 = 1\,\mathrm{mm}^{-0.218}$, and deviates thereafter. The crack initiation angle is also not well predicted for this case. It is important to note that the various failure criteria for this case in Seweryn and Lukaszewicz (2002) also do not match well the experimental results.

5.2 Experiments on three-point-bending specimens made of PMMA

Three point bending (3PB) experiments were conducted on PMMA notched specimens at room temperature loaded so to produce a mixed mode state at the notch tip.

To obtain the material parameters we conducted two flexural tests on PMMA bar samples $80 \times 10 \times 10$ mm (without a notch) at room temperature obtaining σ_{c}=105.8 MPa and $\sigma_{\mathrm{c}} = 117.8$ MPa.

Table 5 H_{ij} for $\omega = 270$ and $240°$ ($E = 1, \nu = 0.36$)

θ_0	$\omega = 270°$			$\omega = 240°$		
	H_{11}	H_{22}	$H_{12} + H_{21}$	H_{11}	H_{22}	$H_{12} + H_{21}$
30°	2.5878	2.4714	4.1873	1.9182	1.4851	2.8891
35°	2.8676	2.4660	4.2622	2.1729	1.5340	3.0419
40°	3.1422	2.4273	4.2538	2.4258	1.5576	3.1330
45°	3.4071	2.3605	4.1586	2.6672	1.5339	3.1272
50°	3.6578	2.2721	3.9755	2.8974	1.4858	3.0418
55°	3.8903	2.1691	3.7059	3.1120	1.4193	2.8760
60°	4.1005	2.0594	3.3540	3.3069	1.3412	2.6319
65^0	4.2848	1.9504	2.9264	3.4786	1.2590	2.3144
70^0	4.4346	1.8601	2.4001	3.6194	1.1764	1.9522
75^0	4.5492	1.7913	1.7977	3.7232	1.0988	1.5743
80^0	4.6220	1.7565	1.2856	3.7979	1.0401	1.1447
85^0	4.6633	1.7540	0.6647	3.8419	1.0041	0.6809
90^0	4.6793	1.7506	3.266E-3	3.8536	0.9875	6.23E-3

Table 6 Experimental load at failure and crack initiation angle according to Seweryn and Lukaszewicz (2002) and predicted results for the V-notch with an angle of $\omega = 320°$

A_2/A_1	Experimental		Prediction		
[mm$^{-0.135}$]	θ_c [deg]	Avg. critical load [N]	θ_c [deg]	Critical load [N]	ℓ_0 [mm]
0.213	75	2013	75	2008	0.0218
0.460	65	2150	65	2118	0.0205
0.797	52	2560	55	2334	0.0190
1.381	48	2656	45	2717	0.0169
2.975	35	3190	35	3399	0.0148

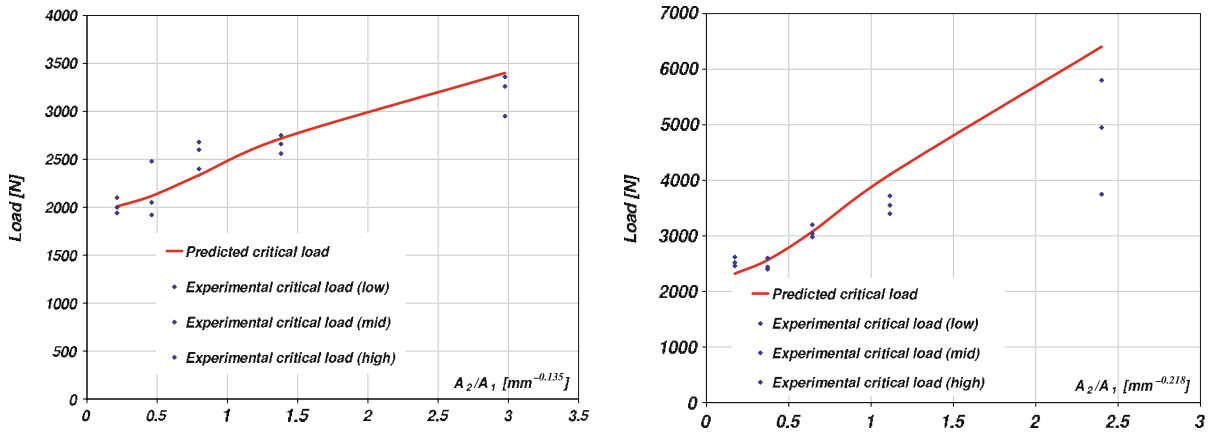

Fig. 11 Predicted and experimental critical load [N] for PMMA specimens Seweryn and Lukaszewicz (2002) with 320° (*left*) and 280° (*right*) V-notch angles

The average values of $E = 3100$ MPa and $\sigma_c = 111.8$ MPa were used in our computations.

We performed also four fracture toughness experiments obtaining $K_{Ic} = 1.03, 1.07, 1.15, 1.25$ MPa $\sqrt{m}$ with an averaged value of $K_{Ic} = 1.12$ MPa $\sqrt{m}$.

The various V-notched samples are all with the same solid opening angle of $\omega = 315°$, a radius of 0.03 mm at the tip and dimensions as shown in Fig. 13).

In Table 8 the different boundary conditions used to generate different mode mixity ratios are

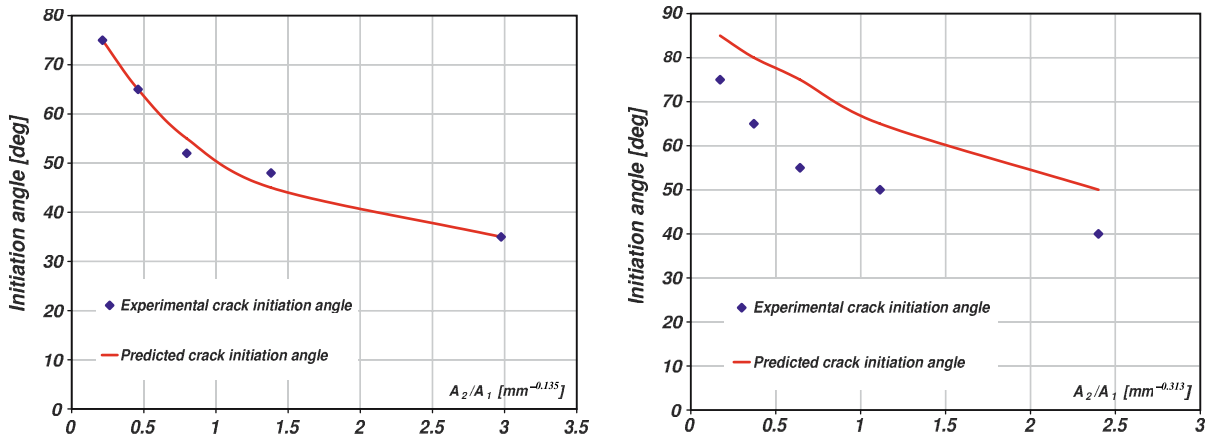

Fig. 12 Predicted and experimental crack initiation angle for PMMA specimens Seweryn and Lukaszewicz (2002) with 320° (*left*) and 280° (*right*) V-notch angles

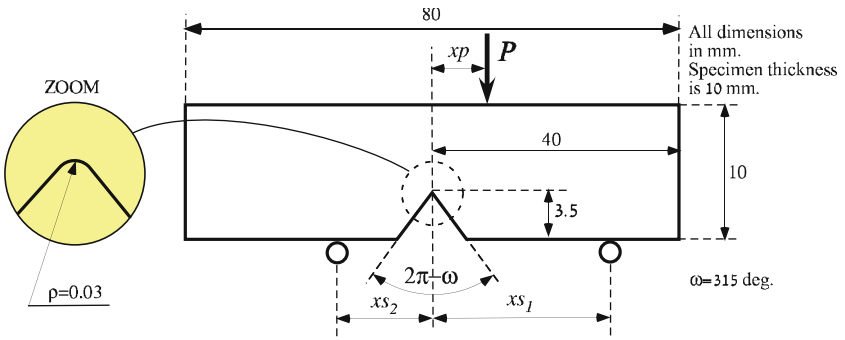

Fig. 13 Dimensions for the PMMA 3PB specimens with 315° V-notch

summarized, and in Fig. 14, we show pictures of the crack created at the V-notch tip in the various specimens.

5.2.1 *Predicted load and crack initiation angle compared to experimental observations.*

We computed according to the proposed criterion the load at failure and crack initiation angles for the tested specimens. This was accomplished by creating *p*-FE models representing the experimental samples.[2] The FE models were constructed according to the dimensions of the same 3PB configuration but with a unit load, having several layers of elements graded in a geometrical mesh refinement in the vicinity of the V-notch angle to reduce the numerical errors. For each experimental configuration the GSIFs at the V-notch tip were extracted from the FE analysis (see a typical FE model in Fig. 10) and the ratio $A_2^{\mathrm{FE}}/A_1^{\mathrm{FE}}$ computed. For the specific load mixity ratio we computed the values of H_{ij}, ℓ_0 $A_{1\mathrm{c}}$ for a range of crack initiation angles $\theta = 90$–$30°$. The angle θ at which the lowest $A_{1\mathrm{c}}$ is obtained is denoted as the crack initiation angle θ_{c} and $A_{1\mathrm{c}}(\theta_{\mathrm{c}})$ as the critical notch GSIF. The predicted critical load can then be computed by the ratio $A_{1\mathrm{c}}(\theta_{\mathrm{c}})/A_1^{\mathrm{FE}}$.

Because K_{Ic}, has an influence on the predicted failure load for V-notches having angles above $\omega = 270°$, we computed failure load at the two limits - for the upper bound of $K_{\mathrm{Ic}} = 1.03\,\mathrm{MPa}\sqrt{m}$ and for the lower bound $K_{\mathrm{Ic}} = 1.25\,\mathrm{MPa}\sqrt{m}$. This provides the higher and lower bounds of the predicted load for fracture $P_{\mathrm{cr}}^{\mathrm{high}}$ and $P_{\mathrm{cr}}^{\mathrm{low}}$, respectively. Note also that in our case the value of σ_{c} has very small influence on the failure loads because in the failure criterion it is given as $\sigma_{\mathrm{c}}^{2\alpha_1-1}$, and because $\alpha_1 = 0.5050097$, it's influence is negligible.

[2] Computations were performed with the *p*-FE code Stress-Check — Trademark of Engineering Software Research and Development Inc., St. Louis, MO, USA

Table 7 Experimental load at failure and crack initiation angle according to Seweryn and Lukaszewicz (2002) and predicted results for the V-notch with an angle of $\omega = 280°$

A_2/A_1	Experimental		Prediction		
[mm$^{-0.218}$]	θ_c [deg]	Avg. critical load [N]	θ_c [deg]	Critical load [N]	ℓ_0 [mm]
0.172	75	2533	85	2320	0.0240
0.371	65	2480	80	2565	0.0244
0.643	55	3070	75	3075	0.0252
1.113	50	3556	65	4101	0.0268
2.400	40	4833	50	6404	0.0303

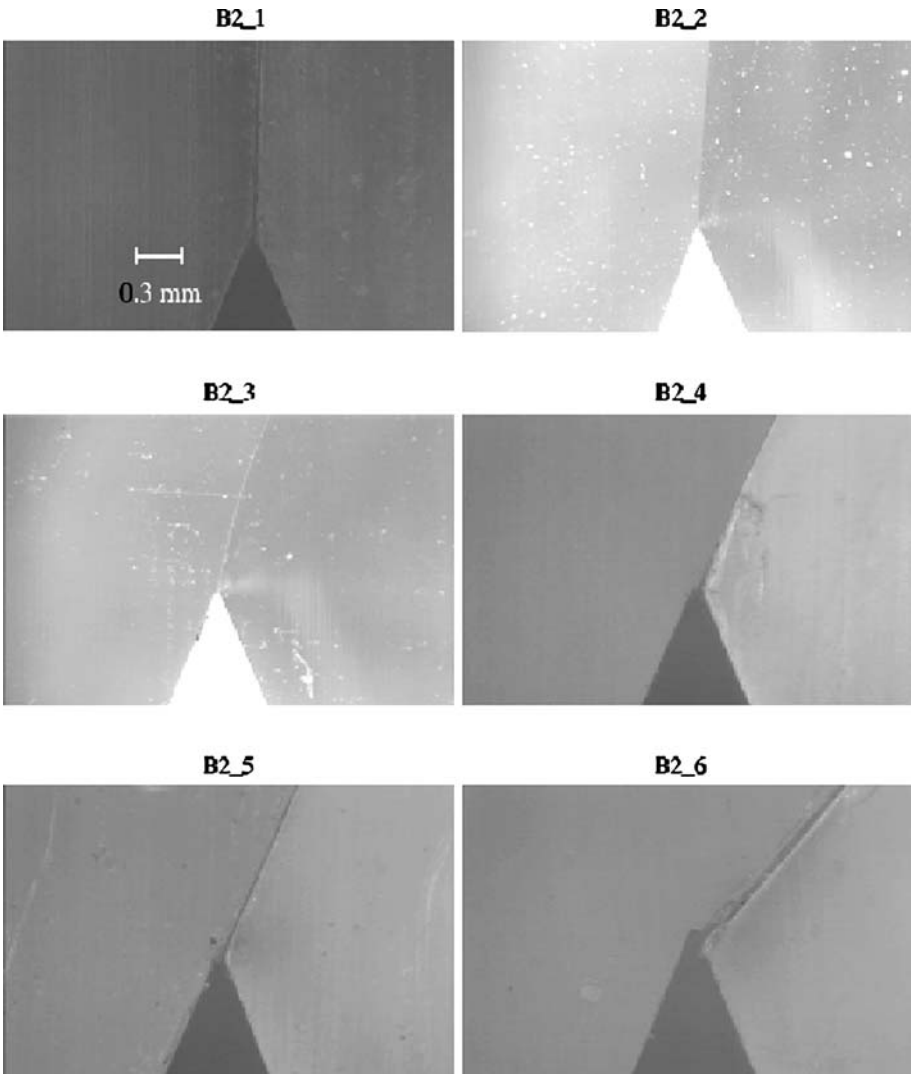

Fig. 14 Pictures of the cracks at the 315° V-notch tip in 3PB PMMA specimens,(scale identical to all pictures)

Table 8 Constrains and loading location for the different PMMA specimens tested

Specimen	Loading configuration [mm]			θ_c [deg]	P_{cr} [N]
	xp	xs_2	xs_1		
B2-2	2	18	22	85	226
B2-3	6	14	26	79	301
B2-4	10	10	30	72	408
B2-5	13.5	6.5	33.5	68	613
B2-6	16	4	36	60	998

Table 9 FE analysis results for 3PB PMMA specimens

Specimen	H_{ij} values for θ_c			A_2/A_1 [mm$^{-0.154}$]	ℓ_0 [mm]	θ_c [deg]	P_{cr}^{high} [N]	P_{cr}^{low} [N]
	H_1	H_2	$H_{12}+H_{21}$					
B2-2	0.00171	0.00101	0.00025	0.073	0.0165	86	200	166
B2-3	0.00170	0.00102	0.00041	0.156	0.0165	82	253	209
B2-4	0.00169	0.00104	0.00056	0.216	0.0164	77	360	298
B2-5	0.00164	0.00108	0.00085	0.333	0.0162	73	537	463
B2-6	0.00154	0.00117	0.00127	0.616	0.0155	63	899	749

Table 10 Constrains and loading locations for the different MACOR specimens tested

Specimen	Loading configuration [mm]				θ_c [deg]	P_{cr} [N]
	xp_1	xp_2	xs_2	xs_1		
M-6	30	0	30	20	70	2,200
M-7	30	10	30	20	46	2,800
M-8	30	13	30	20	43	3,370
M-9	30	15	30	20	33	5,540
M-10	30	17	30	20	27	6,590

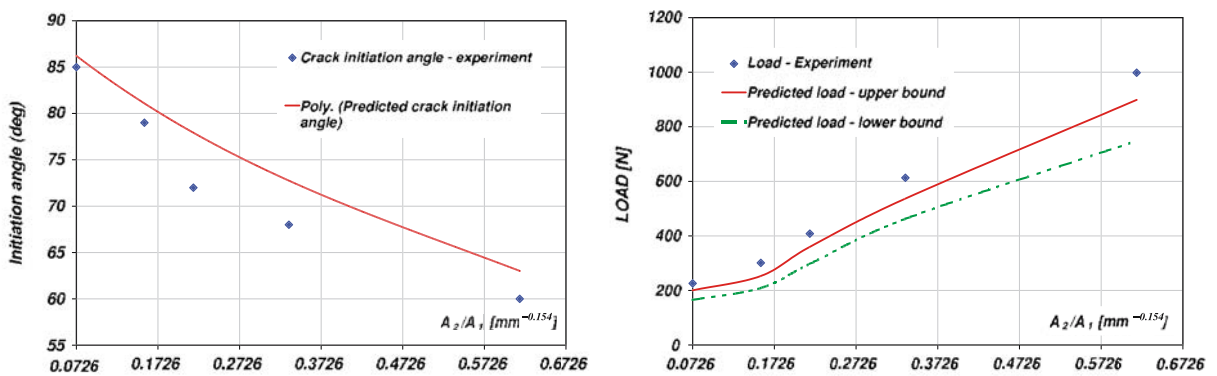

Fig. 15 Predicted and experimental crack initiation angle (*left*) and critical load [N] (*right*) for 3PB PMMA specimens with 315° V-notch angle

We summarize in Table 9 the obtained results, and present these in a graph in Fig. 15.

One may notice the good correlation between the predicted and experimental data. It is expected that the predicted failure load will be lower compared to the experimental results because of the blunt V-notch tip in experiments, whereas the failure criterion assumes a sharp V-notch (see Leguillon and Yosibash (2003) for a correction factor due to notch tip radius).

5.3 Experiments on four-point-bending specimens made of MACOR

Four point bending (4PB) experiments were conducted on Machinable Ceramics (MACOR - manufactured by Aremco) specimens at room temperature loaded so to produce a mixed mode state at the notch tip. Four point bending experiments were done instead of three point bending to achieve a larger mixity ratio.

To obtain the material parameters we conducted flexural tests and ultrasonic inspection on two MACOR bar samples $80 \times 18 \times 10\,\text{mm}$ (without a notch) at room temperature. The values of the Young modulus obtained for the flexural tests were $E = 76532, 77221\,\text{MPa}$ with an average value of $E = 76876\,\text{MPa}$ and the value obtained by the ultrasonic inspection was $E = 66900\,\text{MPa}$. In our computations the value of E obtained by ultrasonic inspections was used because it is regarded as more accurate. We noticed in our computation that the two different Young moduli have very little influence on the failure load and crack initiation angle. One flexural test was conducted in order to obtain the value of the critical stress $\sigma_c = 103\,\text{MPa}$.

To obtain the fracture toughness, we performed two experiments from which, we estimate the range of K_{Ic} to be between K_{Ic} =1.1–1.2 MPa $\sqrt{m}$. This value is smaller than the value reported by the manufacturer $K_{Ic} = 1.53$ (this value is a generic value not obtained from tests on the batch from which the specimens were manufactured).

The various V-notched samples are all with the same solid opening angle of $\omega = 315°$, a radius of 0.03 mm at the tip and dimensions as shown in Fig. 16.

In Table 10 the different boundary conditions used to generate different mode mixity ratios are summarized, and in Fig. 17, we present photographs of the fracture paths emanating at the V-notch tip under the different boundary conditions.

5.3.1 Predicted load and crack initiation angle compared to experimental observations

We computed according to the proposed criterion the load at failure and crack initiation angles. This was accomplished by creating p-FE models representing the experimental samples. The FE models were constructed according to the dimensions of the same 4PB configuration, only that for convenience of modeling the V-notch was indeed V-shaped, not identical to the specimen's "V-notch." We checked that this induced an error of less than 0.1%. In the four point bending tests, because the loading is not symmetric, the forces P_1 and P_2 in Fig. 16 on a sample are not equal. Because in the experiment we prescribed displacements boundary conditions, and measured the resultant force $P_1 + P_2$, we applied displacements boundary conditions on the FE model at the loading points. The value of the displacement was determined so that the resultant force was equal to the load applied in the experiment. For each experimental configuration the GSIFs at the V-notch tip were extracted from the FE analysis and same procedure described for PMMA specimens was followed. We summarize in Table 11 the obtained results.

The lower and upper bounds of the estimated critical loads in Fig. 18 are due to the two values of K_{Ic}. A good correlation between the predicted and experimental data is obtained.

6 Summary and conclusions

The failure criterion of Leguillon at reentrant corners in brittle elastic materials (Leguillon 2002; Leguillon et al. 2003) validated in Yosibash et al. (2004) for mode I loading is being extended herein to mixed mode loading. As in other failure criteria, it requires the knowledge of two material parameters: the critical stress intensity factor K_{Ic} and the strength (in general a peak stress) σ_c

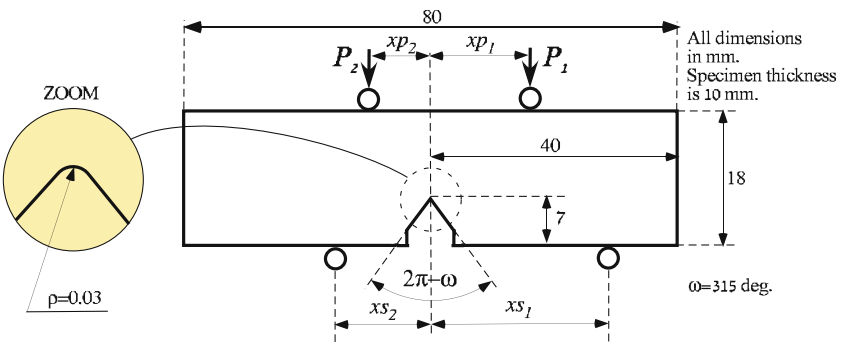

Fig. 16 Dimensions for the MACOR 4PB specimens with 315° V-notch

Table 11 FE analysis results for the MACOR specimens

Specimen	H_{ij} values for θ_c			A_2/A_1 [mm$^{-0.154}$]	ℓ_0 [mm]	θ_c [deg]	P_{cr}^{low} [N]	P_{cr}^{high} [N]
	H_1	H_2	$H_{12}+H_{21}$					
M-6	7.255e-5	4.285e-5	1.060e-5	0.34	0.0182	72.5	2,101	2,287
M-7	7.213e-5	4.328e-5	1.739e-5	1.30	0.0157	50	3,029	3,267
M-8	7.171e-5	4.412e-5	2.376e-5	1.73	0.0148	45	3,845	4,138
M-9	6.958e-5	4.582e-5	3.606e-5	2.20	0.0140	40	4,710	5,058
M-10	6.534e-5	4.964e-5	5.388e-5	3.26	0.0130	35	5,886	6,300

for the material of interest. We provide a rigorous derivation of the extended criterion, which requires a simultaneous satisfaction of the energy release rate and strength criteria, and compute the various ingredients required for the determination of the failure load and crack initiation angle. The validity of the proposed failure criterion is examined by comparing predicted failure loads and crack initiation angles for a range of mode mixity ratios to these measured in experiments. Two sources of experimental results were considered for validating the failure criterion: (a) Experiments performed on PMMA specimens with different V-notch opening angles and mode mixity ratios reported in Seweryn and Lukaszewicz (2002), and (b) Experiments performed by the authors on 3PB V-notched PMMA specimens and 4PB V-notched Macor specimens.

The criterion predicts very well both the failure loads and crack initiation angles for the 320° V-notched specimens made of PMMA under a wide range of mode mixity and a fair prediction of failure loads is noticed for the 280° V-notch specimens made of PMMA reported in Seweryn and Lukaszewicz (2002). Poor prediction of crack initiation angles for the 280° V-notch specimens made of PMMA is observed, however this is consistent with poor predictions of other failure criteria presented in Seweryn and Lukaszewicz (2002) for the same samples and may be a result of an error in the experimental procedure.

A very good predictability is demonstrated for the experiments conducted by us on 3PB 315° V-notched specimens made of PMMA. Because the failure criterion assumes a mathematical sharp V-notched tip the predicted failure loads are expected to be the lower bound to the experimental failure loads, as indeed is the case in Fig. 15. A very good predictability is also demonstrated for the 4PB 315° V-notched specimens made of Macor.

The accuracy of the predicted failure load for PMMA specimens deteriorates as the mode mixity increases. This may be attributed to the non-exact measurement of σ_c, and the blunt tip radius. Future investigations will assess the validity of the failure criterion for a wider range of brittle materials and V-notch angles, as well as the influence of the V-notch tip radius (as done for mode I loading in Leguillon and Yosibash (2003)).

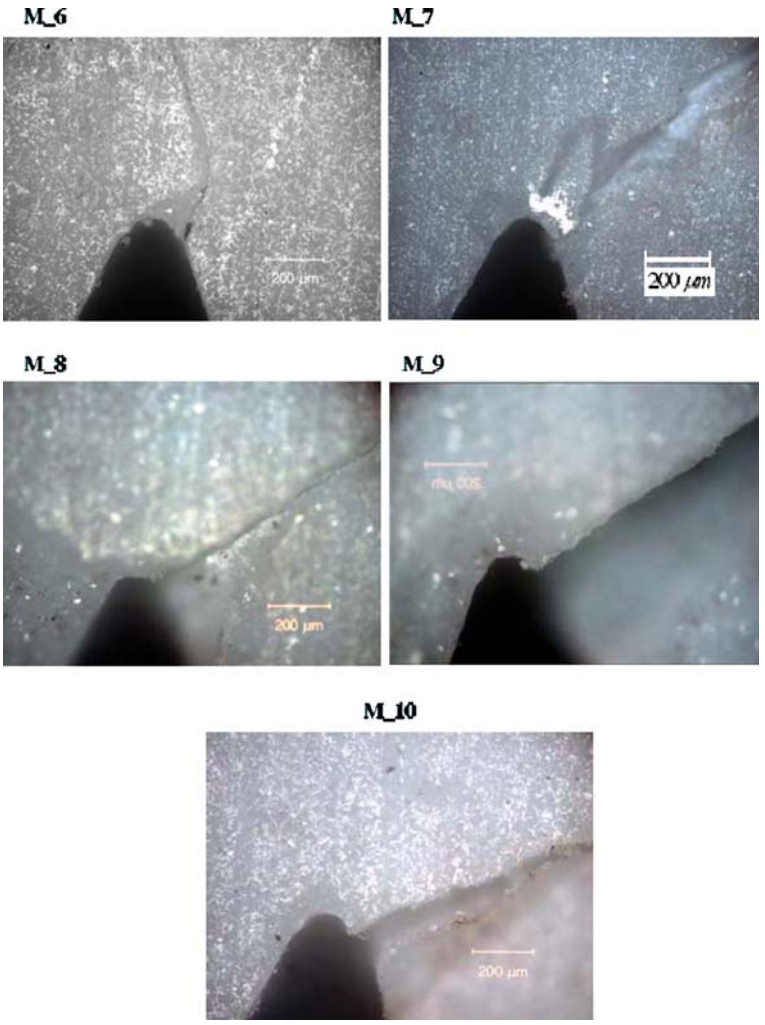

Fig. 17 Photographs of the fracture path at the 315° V-notch tip in 4PB MACOR specimens

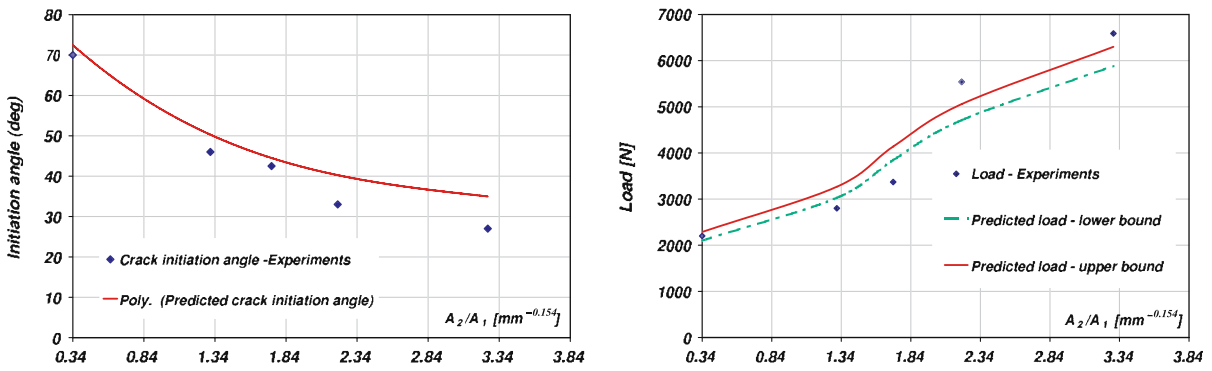

Fig. 18 Predicted and experimental crack initiation angle (*left*) and critical load [N] (*right*) for 4PB MACOR specimens with 315° V-notch angle

Acknowledgements The authors thank Dr. Arie Bussiba and Mr. Moshe Kupiec for their help in performing the experiments and Mr. Ilan Gilad for his help with FE analyses. This research has been partially funded by the VATAT-VEE grant number 86/06.

References

Blum H, Dobrowolski M (1982) On finite element methods for elliptic equations on domains with corners. Computing 28:53–63

Dunn ML, Hui C, Labossiere P, Lin Y (2001) Small scale geometric and material features at geometric discontinuities and their role in fracture analysis. Int J Fract 110:101–121

Dunn ML, Suwito W, Cunningham S (1997a) Fracture initiation at sharp notches: Correlation using critical stress intensities. Int J Solids Struct 34(29):3873–3883

Dunn ML, Suwito W, Cunningham S, May CW (1997b) Fracture initiation at sharp notches under mode I, mode II, and mild mixed mode loading. Int J Fract 84:367–381

Fett T (1996) Failure of brittle materials near stress singularities. Eng Fract Mech 53:511–518

Hashin Z (1996) Finite thermoelastic fracture criterion with application to laminate cracking analysis. J Mech Phys Solids 44(7):1129–1145

Kanninen MF, Popelar CH (1985) Advanced fracture mechanics. Oxford University Press, New-York, NY, USA

Labossiere P, Dunn M, Cunningham S (2002) Application of bimaterial interface corner failure mechanics to silicon/glass anodic bonds. J Mech Phys Solids 50:405–433

Lazzarin P, Zmabardi R (2001) A finite-volume-energy based approach to predict the static and fatigue behavior of components with sharp V-shaped notches. Int J Fract 112:275–298

Leguillon D (2002) Strength or toughness? a criterion for crack onset at a notch. Eur J Mech A/Solids 21: 61–72

Leguillon D, Laurencin J, Dupeux M (2003) Failure initiation in an epoxy joint between two steel plates. Eur J Mech A—Solids 22(4):509–524

Leguillon D, Siruguet K (2002) Finite fracture mechanics Application to the onset of a crack at a bimaterial corner. In: Wales B and Karihaloo (eds.) IUTAM symposium on analytical and computational fracture mechanics of non-homogeneous materials (Cardiff, 18–22 June 2001), solid mechanics and its applications, vol 97. Kluwer Academic Publishers, Dordrecht, pp 11–18

Leguillon D, Yosibash Z (2003) Crack onset at a V-Notch. Influence of the notch tip radius. Int J Fract 122:1–21

Mohammed I, Liechti K (2000) Cohesive zone modeling of crack nucleation at bimaterial corners. J Mech Phys Solids 48:735–764

Reedy JED (2000) Connection between interface corner and interfacial fracture analyses of an adhesively-bonded butt joint. Int J Solids Struct 37:2429–2442

Seweryn A (1994) Brittle fracture criterion for structures with sharp notches. Eng Fract Mech 47(5):673–681

Seweryn A, Lukaszewicz A (2002) Verification of brittle fracture criteria for elements with V-shaped notches. Eng Fract Mech 69:1487–1510

Seweryn A, Poskrobko S, Mróz Z (1997) Brittle fracture in plane elements with sharp notches under mixed-mode loading. J Eng Mech 123(6):535–543

Szabó BA, Babuška I (1988) Computation of the amplitude of stress singular terms for cracks and reentrant corners. In: CTA (ed) Fracture mechanics: nineteenth Symposium. ASTM STP 969, ASTM, Philadelphia, pp 101–124

Taylor D, Cornetti P, Pugno N (2005) The fracture mechanics of finite crack extension. Eng Fract Mech 72:1021–1038

Yosibash Z, Adan O, Shneck R, Atlas H (2003) Thermomechanical failure criterion at the micron scale in electronic devices. Int J Fract 122:47–64

Yosibash Z, Bussiba A, Gilad I (2004) Failure criteria for brittle elastic materials. Int J Fract 125:(3–4) 307–333.